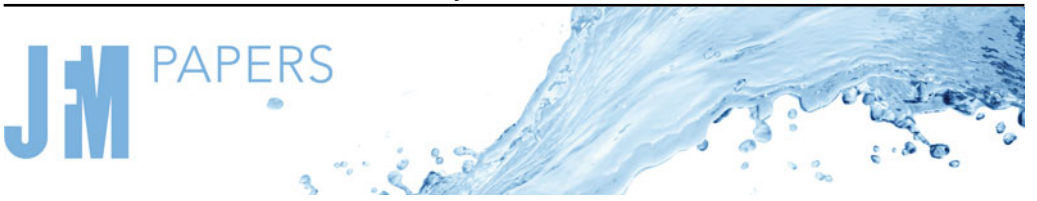
J. Fluid Mech. (2026), *vol.* 1026, A7, doi:10.1017/jfm.2025.10983



On wedge aerated water entry: experiment and theory

Wencheng Wu[1], **Longfei Xiao**[1,2], **Longbin Tao**[3], **Yufeng Kou**[1] and **Yiang Yang**[4]

[1]State Key Laboratory of Ocean Engineering, Shanghai Jiao Tong University, Shanghai 200240, PR China
[2]SJTU-Sanya Yazhou Bay Institute of Deepsea Science and Technology, Sanya 572024, PR China
[3]College of Harbour, Coastal and Offshore Engineering, Hohai University, Nanjing 210098, PR China
[4]Institute of Nuclear Science and Safety, Shanghai Jiao Tong University, Shanghai 200240, PR China
Corresponding author: Longfei Xiao, xiaolf@sjtu.edu.cn

(Received 6 May 2025; revised 12 October 2025; accepted 23 November 2025)

Pre-existing bubbles in the water play a critical role in influencing the impact pressure characteristics during the wedge water entry. This study experimentally and analytically investigates the effect of aeration on water-entry impact. A series of controlled drop tests were conducted using a wedge with a 20° deadrise angle at varying impact velocities and void fractions. Four classical pure water impact models (the Zhao & Faltinsen model (ZFM), original Logvinovich model (OLM), modified Logvinovich model (MLM) and generalised Wagner model (GWM)) were extended to account for the effect of aeration. These modifications accounted for compressibility effects, the time-dependent void fraction, three-dimensional flow corrections and area-averaged pressure calculations, resulting in four modified models (M-ZFM, M-OLM, M-MLM and M-GWM). This marks the first systematic theoretical extension of multiple classical water-entry models to aerated conditions. The proposed models demonstrated good agreement with experimental results, with the M-MLM providing accurate peak pressure predictions and M-GWM performing best in capturing the post-peak behaviours. The results indicated that the expansion velocity of the wetted surface varied spatially and closely matched the M-ZFM predictions. While the peak pressures decreased by up to 32.8 % in highly aerated water, the prolonged impact durations led to a comparable or slightly increased pressure impulse than that in pure water. This finding suggests that prolonged lower-magnitude impacts in aerated water may pose a greater risk to structural safety than short-duration high-magnitude impacts. These contributions offer new physical insight and validated tools relevant to marine engineering design in aerated environments.

Key words: flow-structure interactions, multiphase flow

© The Author(s), 2025. Published by Cambridge University Press.

https://doi.org/10.1017/jfm.2025.10983 Published online by Cambridge University Press

1. Introduction

Scenarios in which a solid impacts a liquid, or conversely, a liquid impacts a solid, are frequently encountered in industrial applications, such as bow or bottom slamming of high-speed vessels (Abrate 2011), the water-entry impact of free-falling lifeboats (Lu, Wu & Zha 2024), aircraft ditching (Iafrati 2016) and the interaction between extreme waves and offshore structures (Shan *et al.* 2025). Significant impact loads are generated during liquid–solid interactions, largely due to the added-mass effect, where a portion of the surrounding fluid is rapidly accelerated by the impacting body upon impact. Extended exposure to these loads poses considerable risks to structure safety, as evidenced by hull damage in vessels and fatigue failures in offshore platforms. In real ocean environments, air bubbles are often entrained in water through various mechanisms (Deane & Stokes 2002), including wave breaking (Melville 1996), melting snow and raindrop impact (Pumphrey & Elmore 1990), resulting in aerated water. With transportation and diffusion processes, the void fraction in the upper seawater layer can reach several per cent (Wu 2000), complicating the water-entry impact problem. Although the hydrodynamic response of water entry in pure water has been extensively studied and is relatively well understood, the mechanisms governing the impact in aerated water remain inadequately clarified. Additionally, most design codes for impact loads on ships and offshore structures are based on pure water environments. Therefore, a deeper understanding of water entry into the air–water mixture is crucial for reducing the risk of structural damage.

Simple geometries of impactors such as the wedge are frequently utilised to derive analytical solutions or perform experiments for understanding the mechanics of water impact. In the pioneering work of von Karman (von Karman 1929), the wedge was selected due to its resemblance to the shape of seaplanes, and a simplified model was proposed for predicting the impact force during seaplane landings by employing momentum conservation and the added-mass effect. This model was later refined by Wagner (1932), who accounted for the water pile-up effect to better determine the wetted surface area. The pressure distribution resulting from water entry is singular at the boundary of the wetted surface. This singular behaviour indicates a concentrated transfer of energy from the rising liquid to the body at the liquid–solid intersection, highlighting the necessity for detailed modelling near the contact line. To address this pressure singularity and improve predictive accuracy, several extensions to the original Wagner theory have been proposed.

The Zhao & Faltinsen model (ZFM) utilised matched asymptotic expansions to incorporate the jet flow near the intersection of the body and the free surface (Zhao & Faltinsen 1993). The original Logvinovich model (OLM) introduced global corrections by adding extra terms to the velocity potential in the contact region of the Wagner solution, ensuring that the flow velocity at the outer domain remained bounded (Logvinovich 1972). Further refinement of the OLM, which accounts for nonlinear effects associated with the quadratic term in the Bernoulli equation and the real geometry of the wetted surface, led to the development of the modified Logvinovich model (MLM) and the generalised Wagner model (GWM) (Korobkin 2004). The similarity solution proposed by Dobrovol'skaya (1969), alongside the integral hodograph method of Semenov & Iafrati (2006), fully considered the nonlinear aspects of water impact and can be applied to wedge bodies with any deadrise angle, while other models were typically limited to wedges with relatively small deadrise angles. However, these two methods can only work for constant speed impact, while the models of ZFM, OLM, MLM and GWM can accommodate varying speed impacts. Although varying speed impacts are more commonly encountered in reality, there were few experimental studies for validating the accuracy of these theoretical

https://doi.org/10.1017/jfm.2025.10983 Published online by Cambridge University Press

models, let alone the studies comparing theoretical predictions of pressure time histories with experimental data.

The theoretical models discussed above have in common that the fluid was assumed incompressible and the effects of air presence were typically neglected. However, in several scenarios, the influence of trapped air cannot be disregarded. For instance, in the early stage of the water impact of a blunt body, a thin air layer is often entrapped between the solid and the liquid, acting as an air cushion that provides a buffering effect (Ermanyuk & Ohkusu 2005; Peters, van der Meer & Gordillo 2013). Several theoretical studies have been dedicated to investigating how the trapped air between the liquid and the solid alters the deformation of the liquid surface prior to a solid–liquid impact event. Verhagen (1967) developed an analytical model for a falling flat-bottomed body with the air cushion beneath it, treating the gas as a one-dimensional, adiabatic and isentropic flow. In this model, the pressure at the plate edges was assumed atmospheric and a three-phase (solid–liquid–gas) interaction was considered. Khabakhpasheva, Korobkin & Malenica (2013) developed a coupled theoretical model to investigate the influence of trapped-air cavities on fluid impact loads acting on corrugated elastic panels, with particular relevance to Liquefied Natural Gas cargo containment systems. The model captures how the compression of the trapped-air cavity interacts with both the elastic deflection of the panel and the evolution of the wetted area. Their results demonstrate that trapped air significantly affects both the magnitude and distribution of impact pressures, especially in the presence of flexible structures. Recently, Jain *et al.* (2021) investigated the water-entry impact of a disk, revealing that air cushioning induced measurable free-surface deflections and that there is a notable free-surface lifting phenomenon associated with the Kelvin–Helmholtz instability. A linear Kelvin–Helmholtz analysis was further performed to predict the critical air velocity and the most unstable wavelength, in agreement with experimental data. Building on this framework, Fan, Jain & Van Der Meer (2024) derived theoretical estimates for the air velocity below both wave-structured and flat disks during entry. The half-body potential flow theory was employed to evaluate the inertial wetting velocity on wave-structured disks, demonstrating that shallow and smooth wave structures could serve as effective passive strategies to mitigate impact loads. Belden *et al.* (2023) explored water-entry impacts involving bodies with recessed, cupped noses. This study proposed models for the cup gas dynamics in the limit of low and high Weber number, which accurately predicted the conditions for air cavity inflation and suppression. Subsequently, Belden *et al.* (2024) studied the transition from spherical to flat impactors, indicating that as the sphere flattened, a thin trapped-air layer increasingly governed the early pressure peak. Meanwhile, the peak force departed from the Shiffman–Spencer sphere theory and was instead captured by an inertial piston model that links gas-layer compression to the growth rate of added mass.

In addition to the entrapped-air layer, considerable attention has been given to aerated water containing many small bubbles due to its practical importance. The presence of entrained bubbles significantly influences both the peak impact pressure and the duration of the impact, which might be attributed to the compressibility of the air–water mixture. One of the earliest theoretical investigations on the impact of aerated water was conducted by Peregrine & Thais (1996), who examined the rapid filling of a cavity with an air–water mixture. By modelling the bubbly liquid as a compressible fluid with a barotropic relation, an analytical solution for the impact pressure on a wall was derived. Noticeable reductions in both background and peak pressures associated with wave impacts were observed, even at low void fractions. Korobkin (2006) later proposed a linear theoretical model addressing the impact of a vertical wall on a partially aerated liquid layer. In this model, the near-wall

https://doi.org/10.1017/jfm.2025.10983 Published online by Cambridge University Press

region containing entrained air was treated as a weakly compressible medium with reduced sound speed, while the outer liquid domain was modelled as incompressible and inviscid. Nonlinear effects arising from bubble oscillations and the dependency of the sound speed on hydrodynamic pressure were neglected. Simplified formulas were derived to predict the initial peak impact pressure and the corresponding time of occurrence. Additionally, the study highlighted the practical challenge of accurately measuring the thickness of the aerated layer and its associated air concentration.

Extending the model developed by Peregrine & Thais (1996), Bredmose, Peregrine & Bullock (2009) introduced a weakly compressible flow model to investigate the role of entrapped air in violent wave impacts. The aerated water was represented as a homogeneous mixture composed of incompressible liquid and compressible gas phases. Numerical simulations of wave impacts against vertical walls exhibited encouraging agreement with experimental observations. However, their approach experienced notable numerical artefacts, manifesting as spurious oscillations in pressure and velocity fields near the air–water interface. Subsequently, Dias, Dutykh & Ghidaglia (2010) further investigated aerated water impact phenomena by developing a fundamental two-fluid compressible model to explore the effects of entrained air in violent aerated flows. Similar to Bredmose *et al.*'s (2009) methodology, a two-fluid barotropic approach was utilised to account for mixture compressibility. The numerical model was validated across several aerated water impact scenarios, including dam-break and drop-impact cases. The numerical model for biphasic mixtures was also employed to simulate breaking waves of varying heights impacting vertical walls, as examined by Bredmose *et al.* (2009), with additional validations against the experimental data provided by Bullock *et al.* (2007). The findings demonstrated that the compressible barotropic model reasonably captures the key features of violent wave impacts observed experimentally. Plumerault *et al.* (2012) developed a fully compressible approach based on a multifluid model, explicitly differentiating among atmospheric air, pure water and dispersed air bubbles within the fluid. This three-fluid framework allows the representation of increased compressibility and density variations caused by aeration. A pressure relaxation technique (Saurel & Abgrall 1999) was adopted for solving the three-fluid model equations. The model's capability to accurately replicate the acoustic properties of bubbly liquids was confirmed through comparisons with the bubbly column experiments performed by Silberman (1957).

In the field of aerated water entry, Ma *et al.* (2016) conducted numerical simulations of a rigid square flat plate entering both pure and aerated water, employing a compressible multiphase flow model. Subsequently, Aghaei *et al.* (2020) carried out a comprehensive numerical study examining the combined effects of aeration and hydroelasticity on the impact forces and the structural response of elastic plates under the assumption of isothermal conditions. Both studies pointed out the dual role of aeration: it can have a beneficial effect on pressures, such as reducing the peak impact pressure, while it can also prolong the duration of loading, potentially inducing additional damage.

Nevertheless, the existing theoretical and numerical studies concerning aerated water impacts have primarily focused on wave impacts, and with relatively little attention paid to the time-dependent evolution of void fraction during the aerated water-entry process involving the continuous generation of bubbles. The dynamic variation in void fraction, which directly affects the bulk density of the fluid and thus the impact loads, remains insufficiently addressed. To fill this gap, the present study modifies the ZFM, OLM, MLM and GWM models to incorporate the effects of aeration, compressibility and the quasi-steady evolution of fluid density through a time-dependent void fraction.

https://doi.org/10.1017/jfm.2025.10983 Published online by Cambridge University Press

Despite the advancements in high-performance computing, measured data remain crucial for quantifying the effect of aeration and validating theoretical models and numerical simulations. Nevertheless, in aerated water-entry scenarios, measuring the void fraction proves challenging, hindering the progress of experimental investigations. Ma *et al.* (2016) conducted a quantitative study on the aerated water impact of a rigid flat plate. Since then, a few experimental studies on the aerated water impact of other body shapes have been conducted, including rigid flat plates (Mai *et al.* 2019; Chuang 2022), the cone (Elhimer *et al.* 2017, 2022) and the disk (Hong, Wang & Liu 2021). Ma *et al.* (2016) and Mai *et al.* (2019) estimated void fractions using a volumetric method, which relied on the assumptions regarding bubble velocity and thermodynamic conditions. Other studies utilised a single optical probe system or fibre optic reflectometer technique to measure void fractions, but these methods are limited to capturing data from a single point.

In this study, the effect of aeration on water-entry impact was investigated experimentally and theoretically. The experimental study was carried out by dropping a wedge from various heights onto the water surface, with aerated water at seven different void fractions. As no prior work has reported wedge aerated water impact data over such a range of velocities and void fractions, this extensive experimental scope represents a pioneering effort in aerated impact studies, which are essential for revealing trends and for robustly validating the theoretical models. A purposely designed conductance-based wire-mesh sensor (WMS) was used to accurately measure void fractions in multiphase flows with high spatial and temporal resolution. A wedge model with a deadrise angle of 20° was chosen as the impactor, as no visible air entrapment was observed upon impact for wedges with deadrise angles larger than 1° (Jain *et al.* 2022). Additionally, the first attempt was performed to model the aeration effect for predicting water-entry impact loads in aerated water by extending existing pure water-entry models (ZFM, OLM, MLM and GWM). These models were modified by incorporating the aeration effect by treating aerated water as a homogeneous mixture of compressible gas (air) and compressible liquid (pure water). The models explicitly introduce time-dependent void fraction expressions based on the added-mass concept, and account for three-dimensional effects and area-averaged pressure distributions. The resulting aerated water impact models were referred to as modified-ZFM (M-ZFM), modified-OLM (M-OLM), modified-MLM (M-MLM) and modified-GWM (M-GWM). The time evolution and spatial distribution of impact pressure were examined in detail along the wedge centreline and the keel direction. Comparative analyses between experimental measurements and model predictions were carried out in pure and aerated conditions to evaluate the accuracy and robustness of the proposed models. Beyond baseline pressure records for consistency and model validation, the present study investigates several quantities in pure and aerated cases: the spatially resolved expansion velocity of the wetted surface, the velocity–pressure scaling and a quantitative characterisation of impact duration and impulse. These analyses illuminate how aeration reshapes both the magnitude and the time history of impact loads and materially enrich the understanding of wedge entry physics in aerated conditions. The quantification of the aeration effect contributed by this study forms a canonical reference for future researchers studying multiphase impacts.

2. Experiment description

2.1. *Experimental set-up*

The water-entry experiments were conducted at the State Key Laboratory of Ocean Engineering of Shanghai Jiao Tong University using a purpose-built drop facility, as shown in figure 1. The drop apparatus and its associated instrumentation are identical to those

https://doi.org/10.1017/jfm.2025.10983 Published online by Cambridge University Press

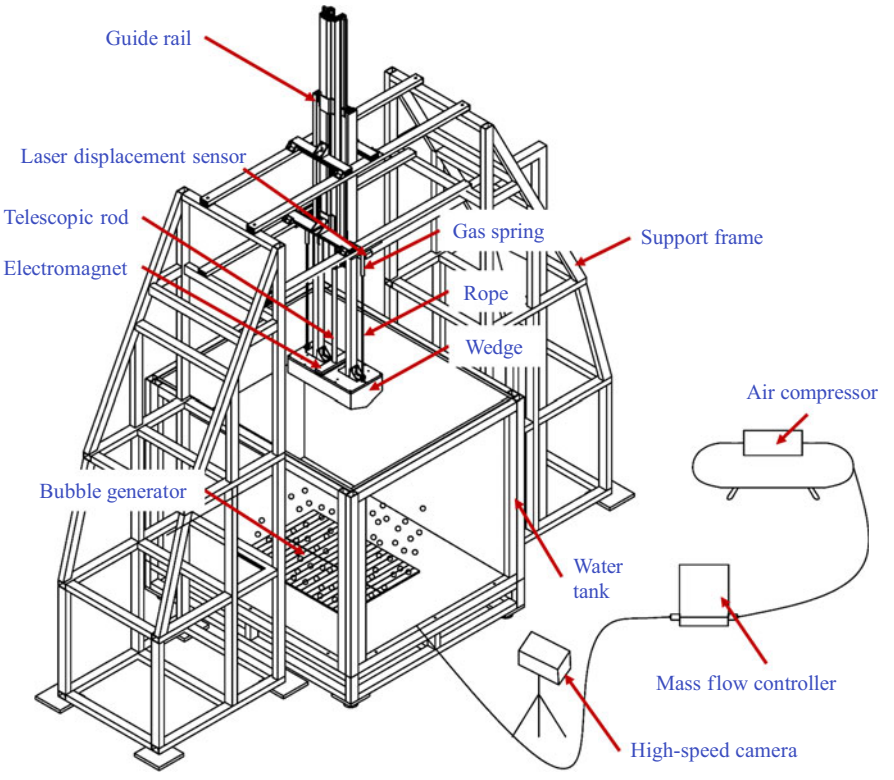


Figure 1. Schematic illustration of the equipment used for aerated water-entry experiments. The experimental set-up is housed within two rigid support frames and consists of a transparent water tank with dimensions of 1.5 m × 1.25 m × 1.2 m, filled to a depth of 0.8 m. A wedge-shaped body, positioned at the centre of the tank, is dropped vertically into the water to study the water-entry impact pressure. A bubble generator is placed at the bottom of the tank to create a controlled aerated environment. The entire water-entry process is captured by a high-speed camera for detailed flow visualisation.

employed in an earlier work by the authors to study the influence of aeration on the impact pressure at one entry velocity (Wu *et al.* 2025). The present work provides a more complete picture of velocity and aeration influences and extends the analysis to additional response quantities, including impact duration, impulse and the expansion velocity of the wetted surface. The experimental set-up featured a transparent water tank with dimensions of 1.5 m in length, 1.25 m in width and 1.2 m in depth, maintaining a consistent water depth of 0.8 m. Structural support was provided by two high-strength steel frames, while a pair of guide rails ensured the wedge's vertical trajectory. As displayed in figure 2, the impactor was an aluminium wedge with a length of 0.50 m, a width of 0.25 m and a deadrise angle of 20°. The total mass of the falling structure, including the wedge and associated support components, was 23.3 kg. An electromagnetic release system, mounted on an electric telescopic rod, allowed precise control of the wedge's initial position.

The impact sequence was filmed using a high-speed camera (FASTCAM SA-Z, Photron) for qualitative flow visualisation. Impact pressures were measured with 24 strain-gauge pressure sensors (PGMC-A-200KPZ15, KYOWA) that were flush mounted with the wedge bottom surface. All the sensors have a sensing area of 8 mm in diameter and a maximum measurement capacity of 200 kPa. The locations and the identification number of pressure sensors are depicted in figure 2. Pressure data were recorded at a 20 kHz sampling rate. The wedge's displacement during the drop was tracked using a laser displacement

https://doi.org/10.1017/jfm.2025.10983 Published online by Cambridge University Press

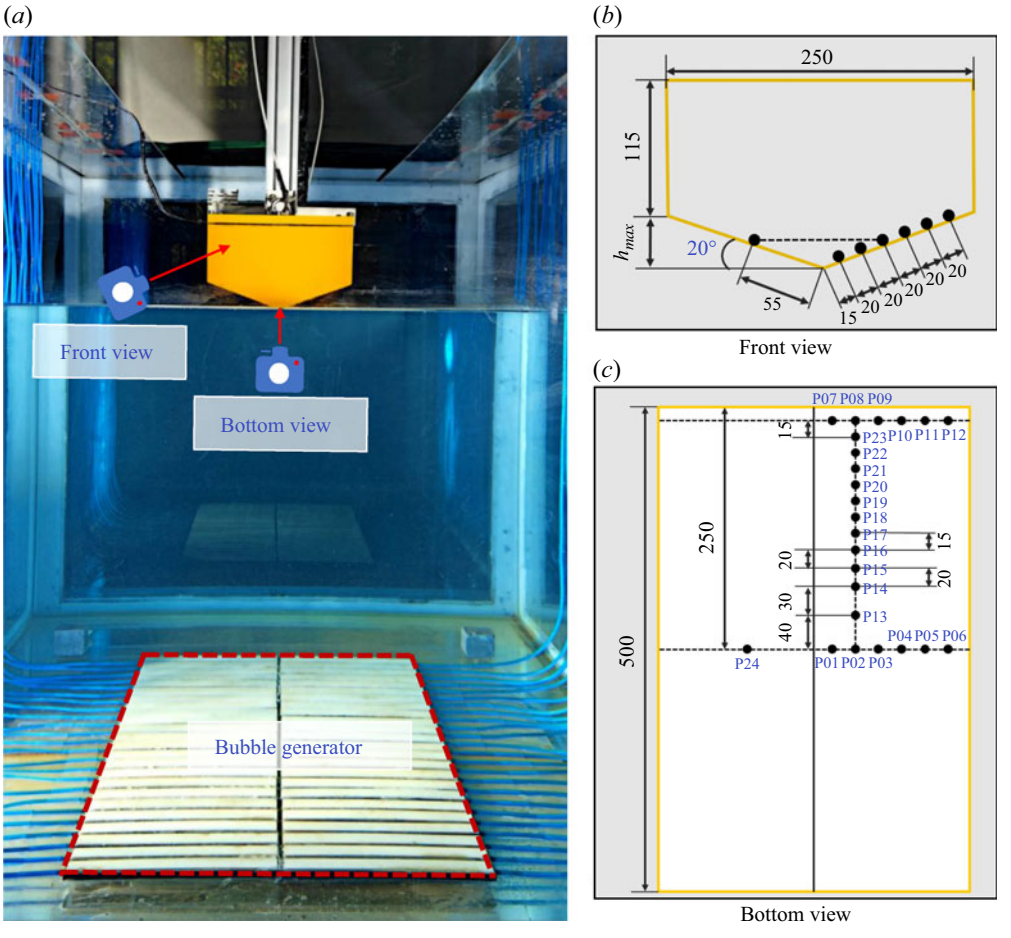


Figure 2. Photograph of the bubble generator and pressure sensor layout on the wedge model. The porous boxes are arranged in a grid-like pattern to ensure uniform bubble generation. Front view (top right) shows the wedge with deadrise angle $\beta = 20°$, indicating the sensor distribution along the inclined surface. Bottom view (bottom right) provides the detailed arrangement of 24 pressure sensors (P01–P24). Sensors P01–P06 were installed along the centreline, and P07–P12 were aligned along the edge of the same side. Sensors P13–P23 were distributed at consistent vertical heights but varying longitudinal positions to capture pressure variation along the wedge face. Sensor P24 was symmetrically placed opposite P03 for validation of experimental symmetry. All dimensions are given in millimetres.

sensor (Y1TA100QXVT80, Wenglor) mounted on a vibration-isolated frame. These data enabled precise calculations of instantaneous velocity and acceleration. The repeatability of the wedge motion and the reliability of the water-entry apparatus are indicated by the consistent impact pressure profiles in figure 3.

A custom-designed bubble generator was employed to create controlled aerated water conditions for studying the effect of void fraction on wedge impact pressure. The system consisted of 48 quartz sand-based porous boxes, arranged in two rows at the bottom of the water tank, as depicted in figures 1 and 2. Each box, measuring 300 mm by 34 mm, featured a quartz top and allowed compressed air to escape through small gaps, forming finely dispersed bubbles. Compressed air was supplied by an air compressor, regulated by a digital mass flow controller (AS200, Aosong) with a range of 0–300 l min^{-1}. This system allowed precise control of the aeration level by adjusting the gas flow rate.

https://doi.org/10.1017/jfm.2025.10983 Published online by Cambridge University Press

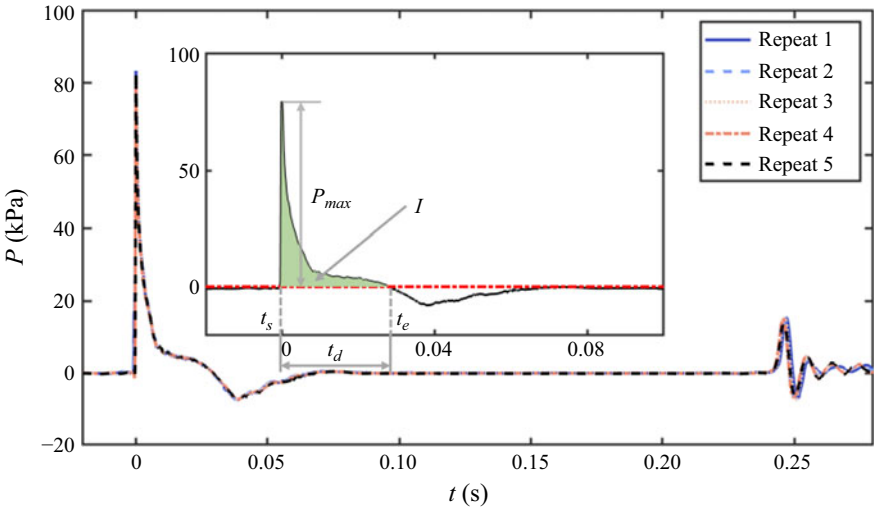


Figure 3. Denoised impact pressure time histories obtained from five repeated tests and schematic diagram of parameter definition. The curves exhibit excellent repeatability of the pressure response during wedge entry. The inset illustrates the method for determining the peak pressure P_{max}, the duration t_d and the corresponding pressure impulse I, calculated as the area under the pressure curve between t_s and t_e.

This set-up ensured repeatable conditions for evaluating the impact of varying aeration on the impact pressure during wedge entry.

Prior to the impact tests, void fraction measurements were performed using a conductance-based WMS. The WMS functions by detecting variations in the electrical conductivity of the fluid between two orthogonally arranged planes of parallel wires. In this study, the purposely designed WMS comprised 64 parallel electrodes per plane with a pitch of 4 mm, forming a measurement matrix of 4096 measuring points (64 × 64 grid). The effective measuring area of the WMS was 256 × 256 mm, slightly larger than the pressure sensor array (less than 250 × 250 mm), thus providing full coverage. The sensor was positioned approximately 0.75 m above the tank bottom to measure the void fraction close to the water's free surface. Data acquisition was carried out at 2500 Hz, with each recording lasting 20 s and repeated ten times for each air flow rate. For additional details on the WMS design and its accuracy validation, please refer to Wu *et al.* (2025).

2.2. *Test conditions*

Pure water entry and aerated water entry were investigated in the present study. Seven different air flow rates were applied: $Q = 0$, 60, 80, 100, 120, 140, 180 l min^{-1}. Table 1 lists the average void fractions and corresponding standard deviations for each flow rate from ten repeated tests measured by the WMS. This experiment considered four distinct drop heights $H = 330$, 520, 750, 975 mm, corresponding to initial water-entry velocities of $v_i = 2.15$, 2.70, 3.24, 3.69 m s^{-1}, respectively. Each test was repeated at least five times for consistent and reliable results. As suggested by Mai *et al.* (2019), a minimum rest period of 15 minutes was allowed between each test to ensure the system stabilised before initiating the next trial.

2.3. *Impact pressure parametrisation*

Given the unavoidable high-frequency noise, a filtering process is required before the raw data can be used to analyse the impact pressure characteristics. A wavelet denoising method was applied to eliminate noise interference from the measurements, which has

https://doi.org/10.1017/jfm.2025.10983 Published online by Cambridge University Press

Air flow rate Q (l min^{-1})	Void fraction α (%)
0	0.00
60	0.80 ± 0.03
80	1.07 ± 0.01
100	1.23 ± 0.04
120	1.35 ± 0.03
140	1.51 ± 0.05
180	1.77 ± 0.02

Table 1. Aeration levels measured by WMS at seven air flow rates.

been proven reliable for processing impact pressure data in previous studies (Guo *et al.* 2020; Zhang *et al.* 2024). The Daubechies-4 wavelet was chosen with 8 decomposition levels, following the universal threshold selection rule as described in Wu *et al.* (2024). All water-entry impact measurements were denoised using this approach.

Figure 3 illustrates the denoised impact pressure time histories obtained from five repeated tests. A distinct initial pressure peak is observed, followed by a secondary peak around $t = 0.24$s. This secondary peak is attributed to the formation of an air pocket at the bottom surface of the wedge at the time when the secondary peak occurs. The trapped air then undergoes multiple cycles of compression and expansion, inducing additional but significantly smaller pressure on the wedge. A detailed explanation can be found in Wu *et al.* (2025). Before the secondary peak, the impact pressure curves exhibited excellent agreement, confirming the high repeatability and reliability of the experimental set-up. After the second peak, minor variations appeared due to the slight differences in the shape and behaviour of the air pocket between individual tests. However, given the relatively low magnitude of the secondary peak, only the first peak pressure and its associated impulse were considered in the subsequent analysis.

To quantitatively account for the aeration effect on impact pressure, this study identifies several parameters to describe the characteristics of the impact pressure, as shown in figure 3.

(i) The parameter P_{max}: peak impact pressure. The maximum pressure measured by one pressure sensor in a water-entry event.
(ii) The parameter t_d: duration, time interval between instants t_s and t_e.
(iii) The parameter I: impact pressure impulse, the integral of impact pressure over the total duration.

The start time t_s and the end time t_e were identified using a threshold set at 1 % of the peak impact pressure P_{max}, minimising the influence of data oscillations. Impact pressure impulse I was determined by integrating the impact pressure over the duration, as shown below

$$I = \int_{t=t_s}^{t=t_e} P \mathrm{d}t. \tag{2.1}$$

3. Modified models for wedge entry with aeration

In this section, modified theoretical models based on Wagner theory are developed to calculate the impact loads experienced by a wedge during entry into aerated water.

https://doi.org/10.1017/jfm.2025.10983 Published online by Cambridge University Press

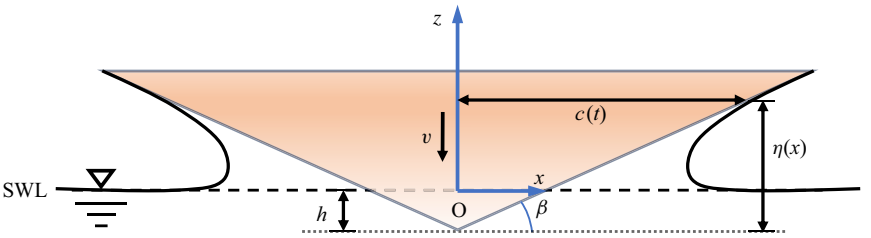


Figure 4. Sketch of the wedge water entry as used in the Wagner model.

Section 3.1 briefly reviews several classical theoretical models for water-entry impact loads, including the original Wagner model, ZFM, OLM, MLM and GWM. Section 3.2 subsequently introduces modified theoretical models which incorporate the aeration effect, treating the aerated water as a homogeneous mixture of compressible gas (air) and compressible liquid (pure water), explicitly presenting the time-dependent expressions for the void fraction and accounting for three-dimensional effects and area-averaged pressures. These models are denoted as M-ZFM, M-OLM, M-MLM and M-GWM, respectively.

3.1. *Classical wedge entry models for pure water*

The Wagner model, one of the most classic models for water-entry impact, focused on the problem of blunt body entering water. It is widely regarded as a successful model, with numerous extensions and modifications developed from it. The basic assumptions of Wagner model are that the fluid is incompressible, inviscid and irrotational. Initially, the liquid is at rest, with its free surface being horizontal ($z = 0$) (Wagner 1932). The origin of the Cartesian coordinate system Oxz is defined at the initial contact point between the body tip and the free surface, as illustrated in figure 4. Additionally, the effects of gravity and surface tension are neglected. As depicted in figure 4, during the wedge entry process, the local water surface elevation near the body rises rapidly, causing premature wetting of the wedge surface. This water pile-up phenomenon represents the key distinction between the Wagner model and the earlier von Karman theory (von Karman 1929). Due to the water pile-up effect, the wetted portion of the wedge surface at a given time t has a length denoted as $2c(t)$, with a maximum rise height relative to the wedge bottom expressed as $\eta(x)$. Wagner employed the flat-plate approximation, which equated the wedge water-entry problem to the impact of a flat plate of width $2c(t)$ subjected to a vertically upward flow, where the flow velocity is equal to the entry velocity$v$. The velocity potential ϕ in Wagner model satisfies the following linear boundary-value problem:

$$\begin{cases} \nabla^2\phi = 0, & \\ \frac{\partial\phi}{\partial z} = -v, & z = 0,\ |x| < c, \\ \phi(x, 0) = 0, & z = 0,\ |x| \geq c, \\ \phi(x, z) \to 0, & \sqrt{x^2 + z^2} \to \infty. \end{cases} \tag{3.1}$$

For brevity, the repeated derivations are omitted. The velocity potential on the body surface is obtained as follows:

$$\phi\,(x, 0) = -v\sqrt{c^2 - x^2},\ |x| < c,\ z = 0. \tag{3.2}$$

Here, c represents the half-width of the wetted region, which depends on the geometry of the entering body. For a wedge characterised by a deadrise angle β, the wetted half-length c is given by

https://doi.org/10.1017/jfm.2025.10983 Published online by Cambridge University Press

$$c\,(t) = \frac{\pi}{2\tan\beta}\int_0^t v\,(t)\,\mathrm{d}t. \tag{3.3}$$

The variable z describes the disturbed free-surface shape

$$z(x,\,t) = f(x) - h(t). \tag{3.4}$$

The shape function of a symmetric wedge is given by $f(x) = x\tan\beta$, and $h(t)$ represents the penetration depth following initial contact with the water surface. The pressure P at any point on the wedge surface is determined by employing the unsteady Bernoulli equation

$$P\,(x,\,z,\,t) = -\rho\frac{\partial\phi}{\partial t} - \frac{1}{2}\rho\,|\nabla\phi|^2 - \rho g z. \tag{3.5}$$

Here, ρ denotes the fluid density, and g is the gravitational acceleration. Wagner indicated that the gravitational effect is negligible compared with the large impact forces generated during water-entry process. Moreover, $\nabla\phi$ can be disregarded, as it is considerably smaller than $\partial\phi/\partial t$. Thus, by linearising the Bernoulli equation, the following expression is obtained:

$$P = \rho\frac{\mathrm{d}v}{\mathrm{d}t}\sqrt{c^2 - x^2} + \rho\frac{vc}{\sqrt{c^2 - x^2}}\frac{\mathrm{d}c}{\mathrm{d}t},\ |x| < c. \tag{3.6}$$

The first term on the right-hand side is referred to as the added-mass term, which is related to the acceleration of the wedge $\mathrm{d}v/\mathrm{d}t$. The second term is known as the impact term, which is associated with the change rate of the wetted length $2\mathrm{d}c/\mathrm{d}t$. Integrating the pressure over the wetted width yields the impact force exerted on the wedge as

$$F = \int_{-c}^{c} P\mathrm{d}x. \tag{3.7}$$

In the Wagner solution, as indicated by (3.6), the impact pressure tends to infinity as x approaches c. This singularity is physically unrealistic, hindering the calculation of peak impact pressure values that can be directly compared with experiments. A notable improvement to address this limitation was proposed by Zhao and Faltinsen. By matching asymptotic expansions, Zhao and Faltinsen derived a composite solution that avoids this singular behaviour, known as the ZFM (Zhao & Faltinsen 1993). To avoid repetition of derivations already well documented, the resulting pressure calculation from their approach is directly provided below

$$P_{ZFM} = \begin{cases} \rho vc\frac{1}{\sqrt{c^2-x^2}}\frac{\mathrm{d}c}{\mathrm{d}t} - \rho vc\frac{1}{\sqrt{2c(c-x)}}\frac{\mathrm{d}c}{\mathrm{d}t} + 2\rho\frac{\sqrt{|\tau|}}{(1+\sqrt{|\tau|})^2}\left(\frac{\mathrm{d}c}{\mathrm{d}t}\right)^2, & |x| \le c(t) \\ 2\rho\frac{\sqrt{|\tau|}}{(1+\sqrt{|\tau|})^2}\left(\frac{\mathrm{d}c}{\mathrm{d}t}\right)^2, & |x| > c(t) \end{cases} \tag{3.8}$$

where δ is an asymptotic jet thickness

$$\delta = 2\pi v^2 c\left(4\frac{\mathrm{d}c}{\mathrm{d}t}\right)^{-2}, \tag{3.9}$$

where τ is a parameter related to x

$$x - c = \left(\frac{\delta}{\pi}\right)\left(-\ln|\tau| - 4\sqrt{|\tau|} - |\tau| + 5\right). \tag{3.10}$$

https://doi.org/10.1017/jfm.2025.10983 Published online by Cambridge University Press

Another significant improvement to the Wagner model has been achieved through the inclusion of higher-order terms derived from a Taylor series expansion in the expression of the velocity potential, alongside the consideration of nonlinear terms present in the Bernoulli equation. This modification ensures that the flow velocity near the boundary of the wetted region remains finite. Prominent models developed based on this approach include the OLM proposed by Logvinovich (1972), the MLM and the GWM introduced by Korobkin (2004). In comparison with the Wagner model, the Bernoulli equation in these extended models includes additional nonlinear terms, enabling the following expression to be formulated:

$$P\left(x,t\right)=\rho\dot{h}^{2}\left(t\right)\left[\frac{\dot{c}}{\dot{h}}\frac{c}{\sqrt{c^{2}-x^{2}}}-\frac{1}{2}\frac{c^{2}}{c^{2}-x^{2}}\frac{1}{1+f_{x}^{2}}-\frac{1}{2}\frac{f_{x}^{2}}{1+f_{x}^{2}}-\frac{\dot{d}}{\dot{h}}\right]+\rho\ddot{h}\left(\sqrt{c^{2}-x^{2}}+f\left(x\right)-h\left(t\right)-d\left(t\right)\right). \tag{3.11}$$

In the equations, the dot notation represents the time derivative; $d(t)$ is a function with two general cases considered: one is $d(t)\equiv 0$, which corresponds to the linearisation of the original Wagner problem at the initial liquid level $z=0$. The second case is $d(t)=f[c(t)]-h(t)$, which corresponds to the linearisation at the jet height. In the OLM, the shape of the object is not accounted for in (3.11). Specifically, the second-order terms related to the small deadrise angle β is neglected and $d(t)\equiv 0$ is assumed, leading to the following expression for the pressure:

$$P_{OLM}\left(x,t\right)=\frac{1}{2}\rho\dot{h}^{2}\left(\frac{\pi}{\tan\beta}\frac{c}{\sqrt{c^{2}-x^{2}}}-\frac{c^{2}}{c^{2}-x^{2}}\right)+\rho\ddot{h}\left(\sqrt{c^{2}-x^{2}}+f\left(x\right)-h\left(t\right)\right). \tag{3.12}$$

The velocity potential in the MLM, compared with the original Wagner model, adds a first-order term obtained by Taylor expansion at the surface of the wedge. This treatment allows the MLM to provide more accurate pressure distributions and impact force for objects with larger deadrise angles. The MLM considers the shape of the object by keeping the second-order term of the deadrise angle, while maintaining $d(t)=0$, resulting in the following expression:

$$P_{MLM}\left(x,t\right)=\frac{1}{2}\rho\dot{h}^{2}\left(\frac{\pi}{\tan\beta}\frac{c}{\sqrt{c^{2}-x^{2}}}-\cos^{2}\beta\frac{c^{2}}{c^{2}-x^{2}}-\sin^{2}\beta\right)+\rho\ddot{h}\left(\sqrt{c^{2}-x^{2}}+f\left(x\right)-h\left(t\right)\right). \tag{3.13}$$

The GWM takes $d(t)=f[c(t)]-h(t)$, and also accounts for the object shape by retaining the second-order term of the deadrise angle, yielding

$$P_{GWM}\left(x,t\right)=\frac{1}{2}\rho\dot{h}^{2}\left(\frac{\pi}{\tan\beta}\frac{c}{\sqrt{c^{2}-x^{2}}}-\cos^{2}\beta\frac{c^{2}}{c^{2}-x^{2}}-\sin^{2}\beta+2-\pi\right)+\rho\ddot{h}\left(\sqrt{c^{2}-x^{2}}+f\left(x\right)-\frac{\pi}{2}h\left(t\right)\right). \tag{3.14}$$

For all three methods, there are regions where the pressure is negative, and the value approaches negative infinity as $x\to\pm c$. This singularity is common to most modified Wagner models. Generally, to ensure that the pressure remains positive, the region considered for impact pressure is limited to a small distance before $x=c$, denoted as point a, where $P[a(t),t]=0$ is the solution. The impact force is then obtained by

https://doi.org/10.1017/jfm.2025.10983 Published online by Cambridge University Press

integrating over the positive pressure regions

$$F = \int_{-a}^{a} P\,(x, t)\,\mathrm{d}x. \tag{3.15}$$

It has been demonstrated that the four models mentioned above are reasonably accurate in calculating the impact pressures of wedge-shaped bodies entering water (Tassin *et al.* 2010; Wang & Faltinsen 2017; Wen *et al.* 2024). However, the existing formulations of these models are only applicable to pure water entry and are not suitable for aerated water conditions. Consequently, in the next subsection, modifications of these four theoretical models (ZFM, OLM, MLM and GWM) will be conducted to consider the aeration effect.

3.2. *Modified wedge entry models with aeration effects*

In the modified model, aerated water is represented as a homogeneous mixture of two immiscible phases, compressible gas (air) and compressible liquid (pure water). A representative volume element is considered, within which the volumes of liquid and gas phases are denoted by V_l and V_g, respectively. The total representative volume V is thus expressed as

$$V = V_l + V_g. \tag{3.16}$$

The void fraction α, representing the volumetric fraction of gas within the representative volume, is defined as

$$\alpha = \frac{V_g}{V}. \tag{3.17}$$

In this study, surface tension effects are neglected. A no-slip condition is enforced between the water and gas phases, implying that both phases share the same velocity field. Furthermore, the representative volume is assumed to be in static equilibrium, and thus the detailed behaviour of individual bubbles and the nonlinear effects associated with air bubble oscillations are not considered. Accordingly, the pressures in the liquid and gas phases, denoted by P_l and P_g, are equal (P). These simplifying assumptions align with those adopted in previous studies on aerated water impact (Peregrine & Thais 1996; Bredmose *et al.* 2009). With this hypothesis, the gas–water mixture is described as a barotropic fluid governed by a single pressure–density relationship.

The gas phase is assumed to be compressible and undergoes isentropic compression. Accordingly, the relationship between density and pressure is expressed as follows (Miller *et al.* 2013):

$$\frac{\partial \rho_g}{\partial P} = \frac{1}{c_g^2} = \frac{1}{a_c \gamma}\left(\frac{P}{a_c}\right)^{\frac{1-\gamma}{\gamma}}. \tag{3.18}$$

Here, ρ_g denotes the gas density, c_g is the speed of sound in the gas and $a_c = P/\rho^{\gamma}$ represents the isentropic constant, where γ is the polytropic index. Specifically, $\gamma = 1$ corresponds to isothermal conditions, while $\gamma = 1.4$ indicates adiabatic conditions. Peregrine & Thais (1996) investigated the influence of the polytropic index and determined that its effect on the impact loads in aerated water is minor. In the present study, the equilibrium radius of bubbles generated in the aerated water was approximately 10^{-3} m. Given that compression occurs significantly faster than thermal exchange during impact, the process can be reasonably approximated as adiabatic. Consequently, a value of $\gamma = 1.4$ was adopted. For validation, additional calculations with $\gamma = 1.0$ (isothermal conditions) were also performed, yielding results closely aligned with those for $\gamma = 1.4$.

https://doi.org/10.1017/jfm.2025.10983 Published online by Cambridge University Press

By integrating (3.18), the variation of gas density ρ_g can be expressed as follows:

$$\rho_g = \rho_{g0}\left(\frac{P}{P_0}\right)^{\frac{1}{\gamma}}, \tag{3.19}$$

where ρ_{g0} denotes the reference ambient gas density, and P_0 is the atmospheric pressure. In this study, ρ_{g0} is set at 1.29 kg m^{-3}, and P_0 at 10^5 Pa. The initial volumes of gas, liquid and mixture are denoted by V_{g0}, V_{l0} and V_0, respectively, while α_0 represents the initial gas void fraction. Upon compression, the volume of the gas phase, V_g, adheres to the adiabatic relationship

$$V_g = V_{g0}\left(\frac{P}{P_0}\right)^{-\frac{1}{\gamma}}. \tag{3.20}$$

The liquid phase is regarded as weakly compressible, and the relationship between its density and pressure is provided by Miller *et al.* (2013)

$$\frac{\mathrm{D}\rho_l}{\mathrm{D}P} = \frac{1}{c_l^2}, \tag{3.21}$$

where c_l denotes the speed of sound in water, which is taken as 1500 m s^{-1} in this study. Integration of (3.21) yields a linear relationship between liquid density and pressure

$$\rho_l = \rho_{l0} + \frac{1}{c_l^2}(P - P_0). \tag{3.22}$$

Here, ρ_{l0} represents the density of water under atmospheric conditions, taken as 1000 kg m^{-3}. The volumetric change in the liquid phase is linked to pressure variations through the linear equation of state

$$\frac{V_l}{V_{l0}} = \left(1 + \frac{P - P_0}{K_{l0}}\right)^{-1}, \tag{3.23}$$

where K_{l0} denotes the bulk modulus of water, defined by $K_{l0} = \rho_{l0}c_l^2$. Combining (3.19) and (3.22), the density of the gas–liquid mixture can be expressed as

$$\rho = \alpha\rho_g + (1 - \alpha)\rho_l. \tag{3.24}$$

An increase in pressure leads to the compression of the gas–water mixture, and the volume ratio V/V_0 can be directly related to the volumetric changes of both gas and liquid phases

$$\frac{V}{V_0} = \frac{V_g + V_l}{V_0} = \frac{V_{g0}}{V_0}\frac{V_g}{V_{g0}} + \frac{V_l}{V_{l0}}\frac{V_{l0}}{V_0} = \alpha_0\frac{V_g}{V_{g0}} + (1 - \alpha_0)\frac{V_l}{V_{l0}}. \tag{3.25}$$

By substituting (3.20) and (3.23) into (3.25), the relationship between the void fraction α and pressure P is obtained

$$\alpha = \frac{V_g}{V} = \frac{\alpha_0 \times \left(\frac{P}{P_0}\right)^{-\frac{1}{\gamma}}}{\alpha_0 \times \left(\frac{P}{P_0}\right)^{-\frac{1}{\gamma}} + (1 - \alpha_0) \times \left(1 + \frac{P - P_0}{K_{l0}}\right)^{-1}}. \tag{3.26}$$

https://doi.org/10.1017/jfm.2025.10983 Published online by Cambridge University Press

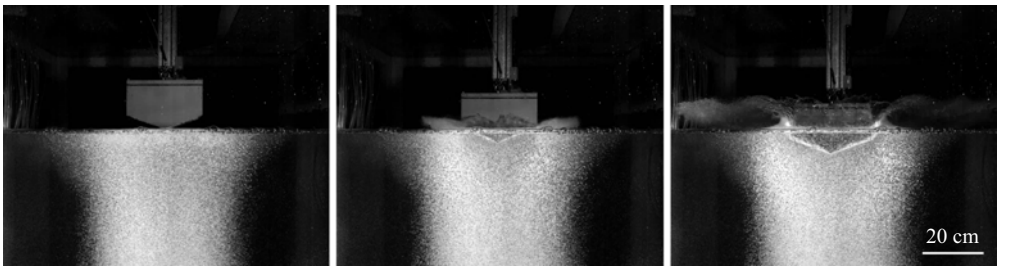


Figure 5. Snapshots of wedge entering aerated water process at different time instants. $t = 0$ms marks the moment when the wedge first made contact with the water surface. The bright white region highlights the distribution and accumulation of bubbles around the wedge as it progressively submerges.

For a homogeneous air–water mixture, the mixture sound speed c_m can be expressed as

$$\frac{1}{\rho c_m^2} = \frac{\alpha}{\rho_g c_g^2} + \frac{1-\alpha}{\rho_l c_l^2}, \tag{3.27}$$

where c_g is the speed of sound in pure air, and c_l is the speed of sound in pure water. The sound speed c_m of the air–water mixture drops dramatically with increasing void fraction. This reduction in sound speed has an immediate effect on the local Mach number, defined as

$$\text{Mach} = \frac{v_e}{c_m}, \tag{3.28}$$

where v_e is the expansion velocity of the wetted surface. A higher Mach number indicates that compressibility effects are more pronounced.

It is worth noting that, in the present study, the highest Mach number achieved is approximately 0.15. The compressibility of the liquid phase has a more negligible effect on the impact loads than that of the gas phase. Within the pressure range considered, the volume change of the gas phase in aerated water is significantly greater than that of the liquid phase. The dominant contribution to the volume change of the aerated water arises from the compression of the gas phase. However, the inclusion of liquid compressibility in the model is intended to enhance the model's robustness and extend its applicability. This consideration may allow the proposed method to remain valid and accurate in scenarios involving higher impact pressures or alternative engineering conditions where liquid compressibility may become comparable to the gas compressibility.

Figure 5 illustrates high-speed snapshots capturing the process of wedge entering aerated water. It can be observed that the brightness distribution on the wetted surface of the wedge appeared relatively uniform and gradually intensified with increasing penetration depth. This observation indicates that bubbles near the wedge surface were approximately uniformly distributed and progressively accumulated as the wedge penetrated deeper. Evidently, the actual void fraction in the region surrounding the wedge during entry significantly exceeded the initial void fraction of the water prior to entry. Consequently, when developing a theoretical model for aerated water-entry impacts, it is essential to consider the temporal variation of the void fraction within the fluid regions close to the wedge surface.

The wedge entry process is governed by the principle of momentum conservation, expressed as

$$Mv + M_a v = Mv_0, \tag{3.29}$$

https://doi.org/10.1017/jfm.2025.10983 Published online by Cambridge University Press

where M represents the mass of the wedge, M_a is the added mass, v is the instantaneous wedge velocity and v_0 is the initial entry velocity. According to the results reported by Yettou, Desrochers & Champoux (2007), the added mass for a three-dimensional wedge entry is given by

$$M_a = C_a \rho' c(t)^2, \tag{3.30}$$

where ρ' denotes the density of the fluid, and the coefficient C_a is defined as

$$C_a = \frac{\pi}{2}\left(1 - \frac{\beta}{2\pi}\right)^2 \cdot \varepsilon. \tag{3.31}$$

In this expression, ε represents a correction factor accounting for three-dimensional effects due to the finite length of the wedge. This correction factor ε is dependent on the ratio of the wetted region width $2c$ to the wedge length L, defined as $K = 2c/L$. Based on the Blagovenshchensky formula (Baarholm 2009), the correction factor ε can be expressed as

$$\varepsilon = \frac{1}{\sqrt{1+K^2}}\left(1 - \frac{0.425K}{1+K^2}\right). \tag{3.32}$$

The concept of added mass arises from the physical phenomenon in which a structure moving through a fluid must accelerate a portion of the surrounding fluid, thereby experiencing an additional inertial force. This effect becomes especially significant during rapid acceleration or deceleration, as in water-entry scenarios. As first proposed by von Karman (1929), the predominant mechanism driving impact loads during water entry is an added-mass effect due to the fluid being displaced by the submerging wedge. Therefore, the added mass can be interpreted as a crucial parameter that characterises the inertial influence of fluid on structural dynamics.

In accordance with Wagner model (Wagner 1932) and associated models (Lin & Shieh 1997; Belden *et al.* 2023, 2024), the fluid region directly beneath the structure is considered as the primary contributor to the impact load. Accordingly, the added mass is typically attributed to this localised region, which dominates the force response during water entry. Consistent with this approach, the present study adopts the same treatment for the added mass. As illustrated in figure 6, the dot-dashed rectangular area directly beneath the wedge denotes the control volume associated with the added mass. Since the void fraction is a volume-based physical quantity, it is meaningful only when defined within a clearly specified finite region, such as the representative volume defined previously. Consequently, it is reasonable to define the void fraction within the control volume associated with the added mass, shown in figure 6. Moreover, given the flat-plate approximation in these theoretical models, the void fraction is assumed to be spatially uniform along the wetted wedge surface at any given time step. An equivalent depth Z_a of the region corresponding to the added mass is obtained as follows, enabling a more accurate quantification of void fraction variation during impact:

$$Z_a = \frac{M_a}{\rho' \cdot 2c(t)} = \frac{C_a \cdot c(t)}{2}. \tag{3.33}$$

At time t_0, let the void fraction be α_0, the equivalent depth of the added-mass region Z_{a0}, and the wetted half-width c_0. After a short interval dt, these become α_1, Z_{a1} and c_1 at time t_1. Given the known α_0 at t_0 and the need to obtain α_1 at t_1, the gas volume balance is performed over the updated control region characterised by the new wetted half-width c_1 and equivalent depth Z_{a1}. The gas volume in this region is $V_0 = Z_{a1} \times 2c_1 \times \alpha_0$

https://doi.org/10.1017/jfm.2025.10983 Published online by Cambridge University Press

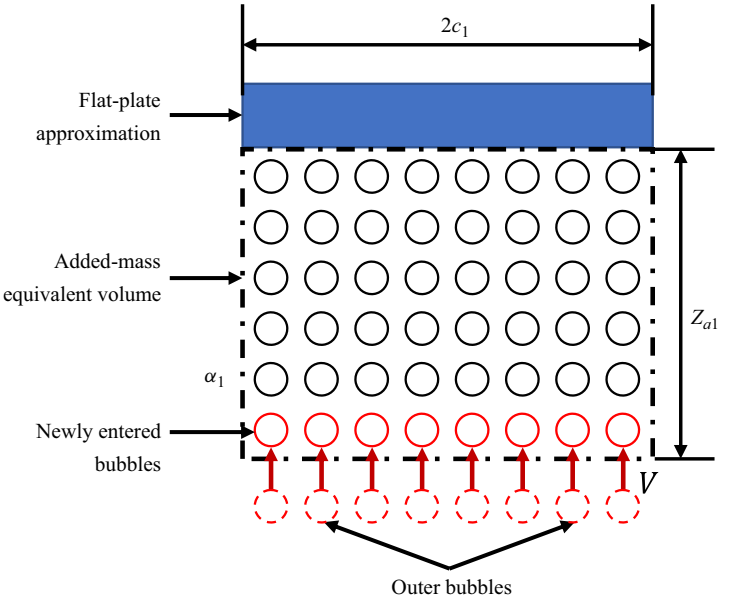


Figure 6. Schematic illustration depicting the determination of the equivalent depth and void fraction calculations during wedge entry into aerated water. Due to the upward motion of the bubbles at relative velocity $V = V_{wedge} + V_{bubble}$, additional bubbles (shown in red dashed circles) enter the considered volume, increasing the gas content. This process updates the void fraction to a new value α_1, capturing the temporal variation of void fraction essential for accurately modelling aeration effects on impact loading.

when evaluated at t_0, and $V_1 = Z_{a1} \times 2c_1 \times \alpha_1$ at t_1. The increase $V_1 - V_0$ represents the additional gas introduced into this volume during dt by bubbles entering from below. The outer bubbles (shown in red dashed circles in figure 6) enter the considered fluid volume ($Z_{a1} \times 2c_1$) with a relative velocity $V = V_{wedge} + V_{bubble}$, contributing an additional gas volume $\Delta V = V\mathrm{d}t \times 2c_1 \times \alpha_0$. Within this short time step, the escape and collapse of bubbles are neglected. The void fraction is then updated by

$$\alpha_1 = \frac{(Z_{a1} + V\mathrm{d}t) \cdot \alpha_0}{Z_{a1}}. \tag{3.34}$$

In this study, bubbles are assumed to be uniformly distributed with a constant rising velocity V_{bubble} of 0.3 m s^{-1}, as determined experimentally by Wu *et al.* (2025), to whom readers are referred for further methodological details.

Furthermore, since the previously described four models are based on two-dimensional theory, three-dimensional effects must be considered for practical wedge geometries of finite length, such as the one in the current study with a length-to-breadth ratio $L/B = 2$. Consequently, the following correction of the impact force for three-dimensional effects is applied:

$$F = F_{2D} \cdot \varepsilon, \tag{3.35}$$

where F_{2D} is the two-dimensional impact force obtained directly from (3.15).

By applying numerical methods and iteratively solving for the void fraction and the effective density of the gas–liquid mixture at each time step, the local pressure at any given instant and location can be determined using (3.8), (3.12), (3.13) and (3.14), which correspond to the ZFM, OLM, MLM and GWM, respectively. Additionally, it should be noted that theoretical models typically yield pressure predictions at a single point on the

https://doi.org/10.1017/jfm.2025.10983 Published online by Cambridge University Press

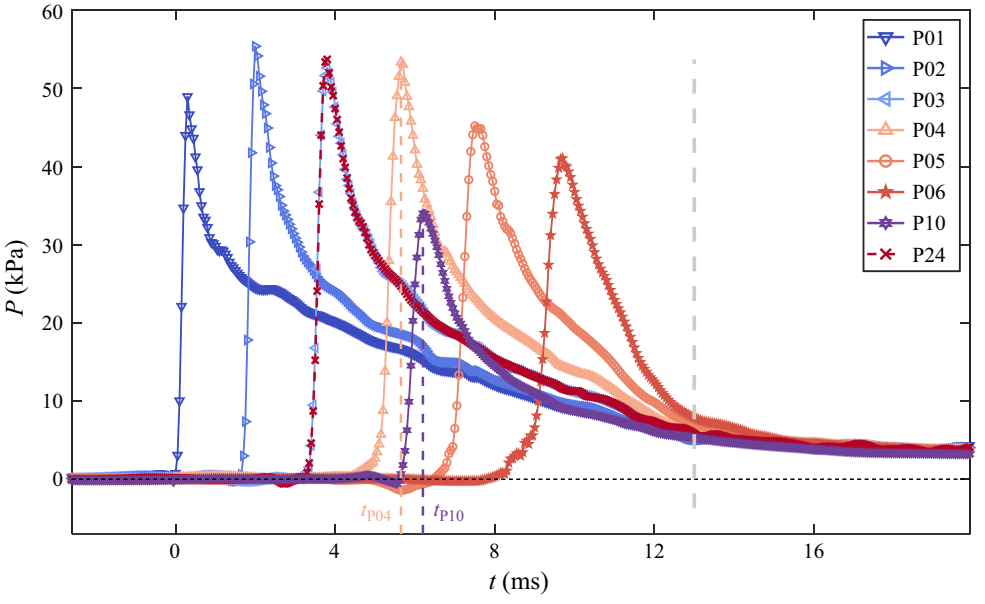


Figure 7. Pressure time series for pure water measured by sensors P01–P06, P10 and P24. The time series were aligned by setting the start time t_s of the first sensor at the keel as $t = 0$, with the start time identified using a threshold set at 1 % of the peak impact pressure. The dashed horizontal black line represents zero pressure, and the dashed vertical grey line denotes the moment of the near-simultaneous pressure drop. Sensors P01–P06 were located along the centreline of one side of the wedge, with each sensor spaced 20 mm apart. Sensors P10 was placed at the same height as P04, but near the wedge edge. Sensors P24 was installed at symmetrical longitudinal and vertical positions relative to P03, but on the opposite side of the wedge.

wedge surface. To facilitate direct comparisons with experimental measurements, an area-averaged pressure corresponding to an 8 mm diameter sensor is calculated.

In summary, by incorporating the enhanced compressibility of the aerated water, the time-dependent variation in void fraction, the aeration effect on gas–liquid mixture density and added mass, along with three-dimensional effects and area-averaged pressure, modified models (M-ZFM, M-OLM, M-MLM, M-GWM) have been developed for wedge entry impact considering aeration effects. These models will subsequently be validated against experimental results to evaluate their accuracy and be further analysed to provide deeper insights into the pressure characteristics during wedge entry into aerated water.

4. Results and discussion

4.1. *Impact pressure time series*

Water-entry impact is regarded as a typical fluid–structure impact phenomenon, with the resulting impact pressure serving as a critical parameter in such interactions. Figure 7 presents typical pressure time series in pure water recorded by sensors P01–P06 (located along the centreline of the wedge), as well as sensor P10 (positioned at wedge edge, aligned with P04 in height) and sensor P24 (placed symmetrically relative to P03 with respect to the keel).

Upon initial contact between the sensors and the water surface, a pronounced pressure spike was generated, lasting of the order of 10^{-3} seconds. As the water surface passed successively over the sensors, the peak pressures were recorded sequentially by sensors P01–P06. Then, a simultaneous decline was detected in the recordings from all the sensors,

https://doi.org/10.1017/jfm.2025.10983 Published online by Cambridge University Press

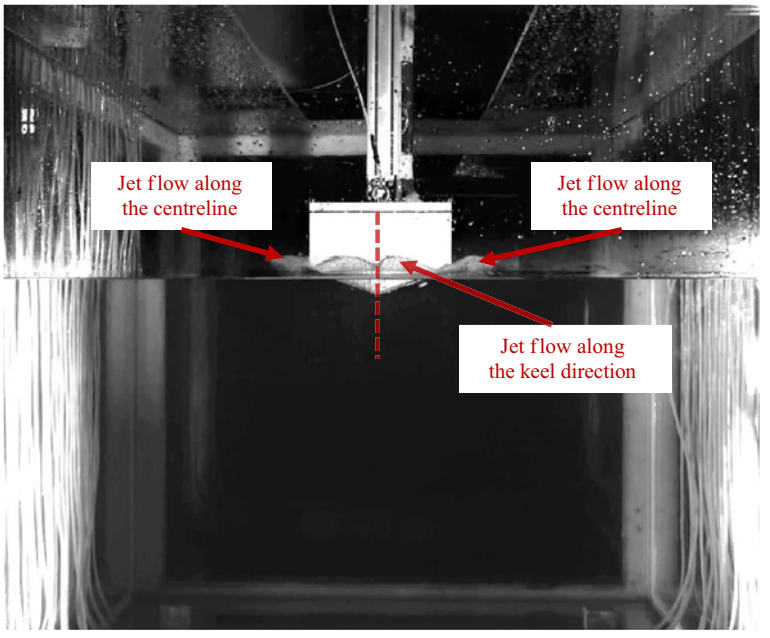


Figure 8. High-speed camera snapshot showing the jet flow development during wedge impact process. The dashed red line marks the symmetry axis of the jet flow, highlighting that the wedge entered the water in a symmetrical way.

as illustrated by the grey dashed line in figure 7. Near-identical pressure profiles were observed between sensors P03 and P24, implying a perfectly vertical and symmetrical entry which was further confirmed by the symmetrical jet flow relative to the red dashed line displayed in figure 8. This agreement highlights the precision of the experimental set-up and further supports the reliability of the results. Comparing sensors located along the wedge's keel with same height, the peak pressure recorded by sensor near edge (P10) is distinctly lower than that measured at centre (P04). Additionally, the timing of the peak pressure for the edge sensor, denoted by t_{P10}, exhibited a measurable delay than the corresponding peak at the centreline t_{P04}. Similar variations were identified when comparing other paired sensors along the keel (P01–P06 and P07–P12). This discrepancy is primarily attributed to the three-dimensional effect of the wedge's interaction with the water, as the wedge behaved as a finite three-dimensional structure, rather than a two-dimensional one as assumed in theories such as Wagner (1932). The water flow became more dispersed at edge, which induced momentum along the keel direction (as shown in figure 8), leading to a delay in the arrival at edge sensor and a subsequent reduction in impact pressure. Therefore, it is crucial to account for the three-dimensional flow effect in the modified analytical models.

Analysis of pressure distributions along the centreline (sensors P01–P06) revealed a nonlinear relationship between the magnitude of impact loads and the proximity to the wedge's keel, characterised by an initial rise followed by subsequent decay. This trend aligned with experiments by Barjasteh, Zeraatgar & Javaherian (2016), who investigated symmetric wedge entry (deadrise angles ranging from 5° to 30°) using 9 mm diameter pressure sensors. In contrast, Yettou, Desrochers & Champoux (2006) employed free-falling wedges with deadrise angles of 15° to 35° and reported that the impact pressures, measured by 19 mm diameter sensors, attained maximum values closest to the keel. Such

https://doi.org/10.1017/jfm.2025.10983 Published online by Cambridge University Press

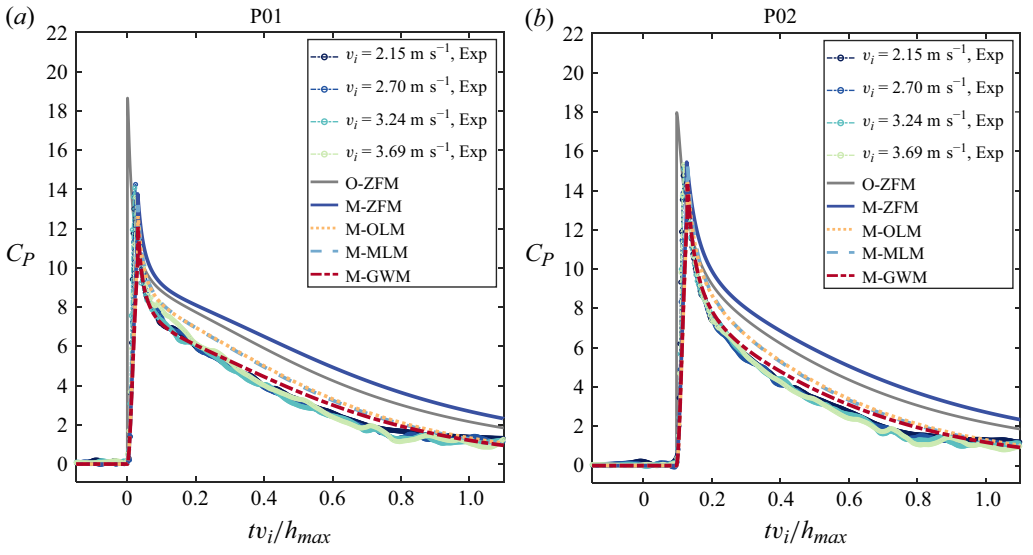


Figure 9. Evolution of impact pressure coefficient C_P for a range of water-entry velocities in pure water, obtained from both theoretical models and model tests. Panel (*a*) shows the results for sensor P01, while panel (*b*) displays the results for sensor P02. The theoretical predictions are based on five models: O-ZFM (grey solid curve), M-ZFM (blue solid curve), M-OLM (orange dotted curve), M-MLM (green dashed curve) and M-GWM (red dash-dotted curve). The phases of the data have been adjusted so that at $t = 0$, the pressure at P01 starts to rise.

conflicting spatial distributions emphasise the sensitivity of pressure measurements to sensor dimensions and positioning. Specifically, the finite sensing area inherently averages local pressure gradients, while variations in sensor size and installation position across studies amplify discrepancies through spatial averaging effects. Consequently, from an experimental perspective, the variation of impact pressure with respect to the distance from the keel can hardly be described by a unified deterministic model in the absence of point pressure sensors – a capability currently unattained due to technological limitations in sensor miniaturisation. These findings are consistent with earlier work by Chuang (1966) and Yamamoto, Ohtsubo & Kohno (1984), which similarly emphasised the lack of a systematic trend in the variation of peak pressures from locations near the keel to those further away.

To validate the applicability of the theoretical models presented in § 3, figure 9 displays the evolution of impact pressure coefficient C_P at sensors P01 and P02 predicted by five analytical models, together with the experimental data for varying water-entry velocities in pure water. Here, h_{max} refers to the vertical distance from the keel to the knuckle of the wedge. The data were adjusted in time so that at dimensionless time $tv_i/h_{max} = 0$ the pressure at sensor P01 begins to rise, with the model calculations adjusted accordingly. Notably, the peak pressure was over-predicted by original Zhao & Faltinsen model (O-ZFM). A gradual reduction in peak impact pressure was observed along the centreline in the O-ZFM model, which contrasted with the experimental trend. Moreover, the impact pressure from O-ZFM exhibited an extremely rapid, near-singular rise, a phenomenon not matched by the pressure time history from the model test. This disagreement arises primarily from the point-based pressure prediction in O-ZFM, combined with its failure to account for three-dimensional flow effect.

From figure 9 it is evident that, until the attainment of the peak impact pressure, the temporal evolution of impact pressure was accurately captured by all four modified models,

https://doi.org/10.1017/jfm.2025.10983 Published online by Cambridge University Press

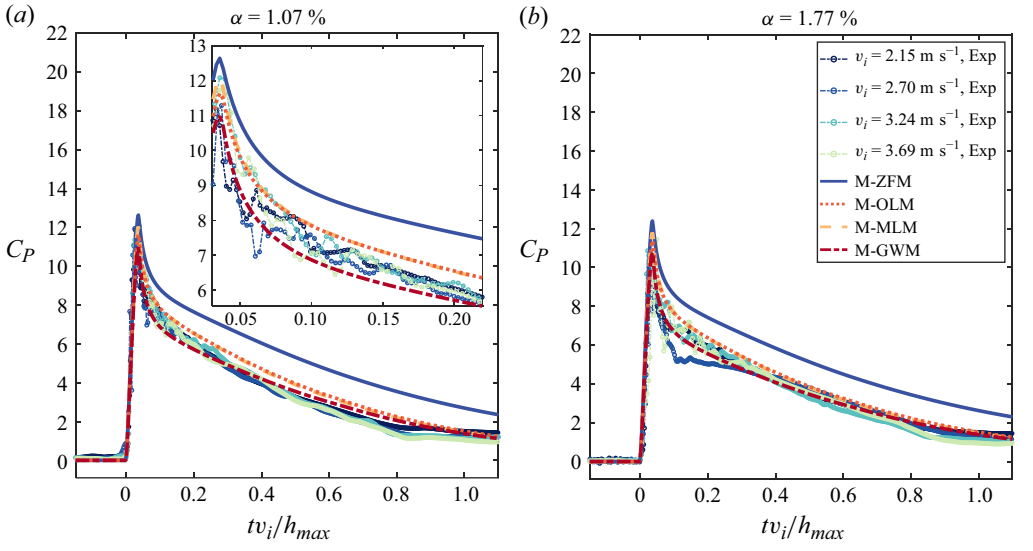


Figure 10. Dimensionless impact pressure C_P time histories at sensor P01 predicted by modified theoretical models (M-ZFM, M-OLM, M-MLM, M-GWM) under aerated water conditions. Panels (*a*) and (*b*) correspond to moderate ($\alpha = 1.07\,\%$) and high ($\alpha = 1.77\,\%$) void fractions, respectively. The inset in (*a*) displays a zoomed-in view of the post-peak pressure region, highlighting the oscillations observed in the experimental pressure measurements. The experimental data are plotted for entry velocities (v_i) ranging from 2.15 to 3.69 m/s. As plotted earlier, time series are shifted so that the point at which the reading on pressure sensor P01 starts to rise lies at $t\,v_i\,/\,h_{max} = 0$.

showing a more gradual pressure rise compared with the O-ZFM. In pure water, the four refined models, which take into account the area-averaged pressure corrections and three-dimensional flow effects, generally demonstrated improved predictive accuracy for peak pressure magnitudes, with the M-ZFM delivering superior agreement with experimental data. The predictive accuracy of the peak pressures in both pure water and aerated water will be discussed in further detail in § 4.3. However, as the immersion depth increased, more pronounced discrepancies in the pressure time series were observed, as illustrated in figure 9. Although the M-OLM and M-MLM models tended to overestimate the pressure time series after the peak, their temporal profiles were in closer alignment with experimental trends than those of the M-ZFM. Notably, the M-GWM model achieved the highest fidelity to experimental measurements during the post-peak period. This enhanced predictive capability may be attributed to the integration of body geometry into the Bernoulli equation and the linearisation of the original Wagner problem at the splash-up height, enabling more physically consistent modelling throughout the entire impact process. Further validation was provided by the temporal delay in pressure rise between sensors P01 and P02, which was successfully reproduced by all modified models.

Accurate prediction of impact loads in aerated water is also critical, as aeration of the water–air mixture is common in open seas. Figure 10 presents the dimensionless impact pressure at P01 calculated by different models and measured during impact tests under moderate ($\alpha = 1.07\,\%$) and high ($\alpha = 1.77\,\%$) void fraction conditions. The phases of the data had been appropriately adjusted to ensure that $t = 0$ aligned with the start time t_s of the pressure rise at sensor P01. Consistent with the pure water case, the modified models closely replicated both the peak pressure and pre-peak pressure rise characteristics in aerated conditions. A reduction in peak pressure is evident in aerated water compared with pure water.

https://doi.org/10.1017/jfm.2025.10983 Published online by Cambridge University Press

Figure 11 further illustrates the temporal evolution of errors between the model predictions and experimental measurements of the dimensionless pressure coefficient C_P, plotted as a function of the normalised time $t v_i / h_{max}$. Notably, the post-peak pressure time series exhibited marked deviations: while the M-GWM maintained good agreement with experimental trends (relative errors generally below 10 %), the M-ZFM was again shown to overpredict the post-peak pressures, as clearly depicted in figure 11. The deviations may be due to the inherent limitations in the ZFM, specifically the neglect of the quadratic velocity term in Bernoulli's equation within the outer solution, and the unsatisfactory treatment of the body boundary condition in the outer flow solution. Fortunately, the accuracy of the peak pressure was not significantly affected, as detailed in § 4.3. Unlike in pure water, the M-OLM and M-MLM achieved post-peak predictive accuracy comparable to the M-GWM in aerated water. This suggests that under aerated conditions, aeration effects play a more dominant role in governing post-impact pressure dynamics than both the location of velocity potential linearisation and the geometric fidelity of the wetted surface.

In comparison with pure water cases, the pressure oscillations observed following the peak were more pronounced in aerated water, as highlighted in the inset of figure 10. The period of these oscillations corresponds closely to the natural pulsation frequency (Minnaert frequency) of the millimetric air bubbles in the aerated water, as demonstrated by Wu *et al.* (2025). The oscillations can be interpreted as bubble pulsations: immediately after impact, compressed bubbles expand and contract, creating damped pressure fluctuations. Because the bubbles in the mixture have a distribution of sizes and are not oscillating in unison, the resulting pressure oscillations are largely stochastic and non-deterministic in nature, as evidenced by the marked reduction in amplitude after ensemble averaging of repeated tests (Wu *et al.* 2025). Such oscillations were not observed in the theoretical results, which explains the larger errors observed near the peak pressure regions depicted in figure 11. This discrepancy stems from the model simplifications employed in the theoretical approach, wherein the water was modelled as a homogeneous, uniformly aerated mixture without explicitly considering the detailed behaviour of individual bubbles. These simplifications were necessary, as modelling the unsynchronised expansion and compression of numerous bubbles, along with random effects, pose substantial challenges for accurate theoretical representation.

4.2. *Expansion velocity of wetted surface*

The expansion velocity of the wetted surface (v_e) is a critical parameter governing hydrodynamic impact dynamics, as it directly quantifies the propagation rate of the liquid–solid interface. One of the key contributions of Wagner theory was the definition of the wetted surface half-length $c(t)$ for specific geometries. This foundational concept has been adopted in subsequent Wagner-based theoretical models, which establish a deterministic functional relationship between impact pressure and $c(t)$, as shown in (3.8), (3.12), (3.13) and (3.14) in § 3.1. For a wedge with a deadrise angle β, $c(t)$ is defined as

$$c(t) = \frac{\pi v_i t}{2 \tan \beta}, \tag{4.1}$$

where v_i denotes the water-entry velocity and β is the wedge deadrise angle. Considering the real geometry of the wedge and constant entry velocity v_i, the expansion velocity of the wetted surface v_e along the wedge can be obtained from Wagner's definition of $c(t)$ as

$$v_e = \frac{\mathrm{d}c(t)}{\mathrm{d}t} \cdot \frac{1}{\cos \beta} = \frac{\pi v_i}{2 \sin \beta}. \tag{4.2}$$

https://doi.org/10.1017/jfm.2025.10983 Published online by Cambridge University Press

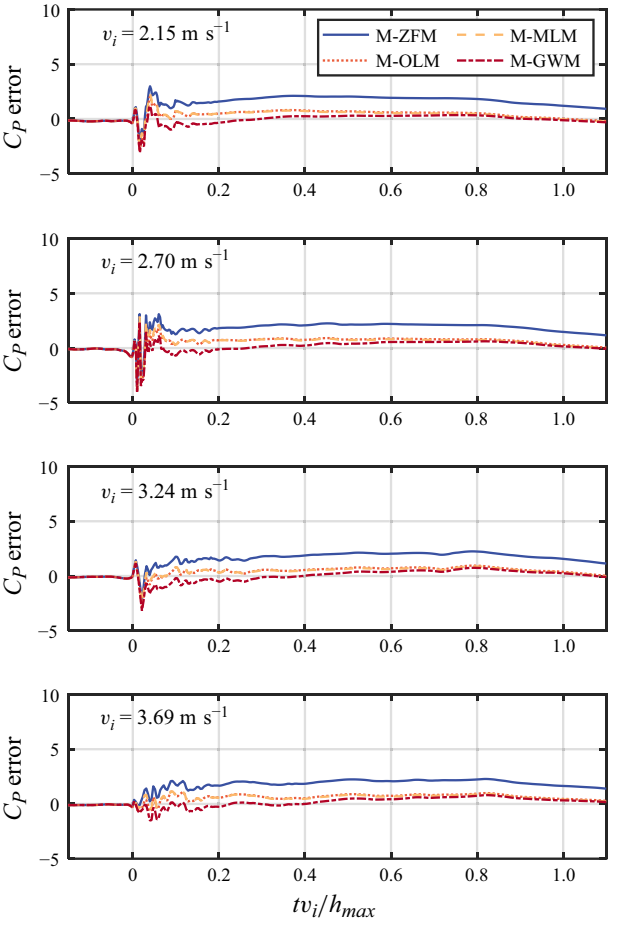


Figure 11. The error between model predictions and experimental measurements of the dimensionless pressure coefficient C_P as a function of normalised time tv_i/h_{max} for $\alpha = 1.07$ %. The error is defined as $C_P^{model} - C_P^{exp}$. Results are presented for four different impact velocities $v_i = 2.15, 2.70, 3.24, 3.69$ m/s, shown from top to bottom. Obviously, the M-OLM, M-MLM and M-GWM demonstrate better agreement with the experimental data, particularly in the post-peak region. In the vicinity of the pressure peaks, noticeable fluctuations in the error are observed, primarily due to the oscillations present in the experimental pressure. A more detailed comparison between the experimental and predicted peak values is provided in § 4.3. It is also noted that within the peak region, the agreement could be further improved by applying a slight time shift.

For all the experimental results, the expansion velocity v_e within the range of the first and last sensors was determined by tracking the position of the jet using the first pressure spike recorded at each sensor. Let x_{01} and x_{02} denoted the positions of sensors P01 and P02, respectively, with t_{P01} and t_{P02} representing the corresponding times to peak pressure. The local expansion velocity between sensors P01 and P02 (v_e^{12}) was calculated as

$$v_e^{12} = \frac{(x_{02} - x_{01})/\cos\beta}{t_{P02} - t_{P01}}. \tag{4.3}$$

This methodology was applied to adjacent sensor pairs along the wedge centreline (P01–P06), yielding five independent expansion velocities (v_e^{12}, v_e^{23}, v_e^{34}, v_e^{45}, v_e^{56}). Similar calculation was performed for the sensors at the edge (P07–P12). Figure 12(*a*) and 12(*b*)

https://doi.org/10.1017/jfm.2025.10983 Published online by Cambridge University Press

depict the measured expansion velocity v_e along the wedge in the central (P01–P06) and edge (P07–P12) regions, respectively. Each column of hollow markers in figure 12 represents the v_e values from five repeated trials at a specific void fraction (α) and entry velocity (v_i), while solid markers indicate the corresponding mean values. Theoretical results from the Wagner model (4.2) and the M-ZFM (derived from (4.3) using predicted impact pressure histories) are also plotted for comparison.

One observes that the Wagner theory overestimated the v_e in both the central and edge regions. This discrepancy arose primarily from the assumption of a constant water-entry velocity, a simplification commonly adopted in many other experimental studies and theoretical models. The constant velocity assumption failed to account for the varying dynamics during impact, leading to a higher predicted expansion velocity and thereby the impact pressure. In contrast, the M-ZFM presented in this study aligned well with the measured expansion velocity in the central region, with the error being less than 4 % in pure water. As shown in figure 9, the time interval between the peak pressures at sensors P01 and P02 was also well captured by the theoretical model, which accounts for varying entry velocities.

The expansion velocity at the edge was generally lower than that at the centre. Near the edge, jet flow momentum dispersed laterally, inducing a horizontal velocity component that diverted energy from the primary wetting surface development along the wedge. As a result, the expansion velocity at the edge was significantly lower compared with the central region, highlighting the importance of considering the spatial variation in jet flow dynamics.

In the experiment, the introduction of aeration inevitably caused minor surface disturbances, potentially leading to slight variations in the initial water contact timing at the sensors, and thereby introducing small errors for calculating v_e. However, as depicted in figure 12, the mean expansion velocities for all void fractions remained relatively consistent, with fluctuations kept within 10 %. Furthermore, the expansion velocity predicted by M-ZFM, developed under the assumption of a flat water surface, remained constant across all tested void fractions for a certain entry velocity, and compared well with the experiments in the central region with a maximum error of less than 10 %. This alignment suggests that the disturbances in the water surface due to aeration are within an acceptable range.

4.3. *Peak impact pressure*

An analysis of the peak impact pressure characteristics was conducted to examine the effects of impact velocity and initial void fraction on impact load during water entry. Figure 13 plots the peak impact pressures P_{max}, averaged from five repeated impact tests for each test condition (characterised by v_i and α), as recorded by sensor P01. From the figure, P_{max} was found to scale linearly with the square of the velocity v_i^2 in pure water, consistent with the expectations for an inertia impact process. A similar scaling behaviour was also reported by Han *et al.* (2024) using free-falling wedges with deadrise angles of 20°, 30° and 45° in pure water. Additionally, the linear relationship persisted in aerated water ($\alpha = 0.80\,\%{-}1.77\,\%$), with only a few points at high entry velocities deviating from the linear trend. This deviation may be due to the limited temporal resolution of the pressure sensor. The slopes of the linear fits of the $P_{max} - v_i^2$ curve decreased with increasing void fraction. For pure water ($\alpha = 0.00\,\%$), the slope measured 7.08 whereas it decreased to 4.49 at $\alpha = 1.77\,\%$. In an inertia-dominated impact process, the slope of the $P_{max} - v_i^2$ relationship for a given wedge geometry is primarily governed by the effective density of the impacting fluid. The observed reduction in slope demonstrated that the introduction of gas bubbles lowered the density of the air–water

https://doi.org/10.1017/jfm.2025.10983 Published online by Cambridge University Press

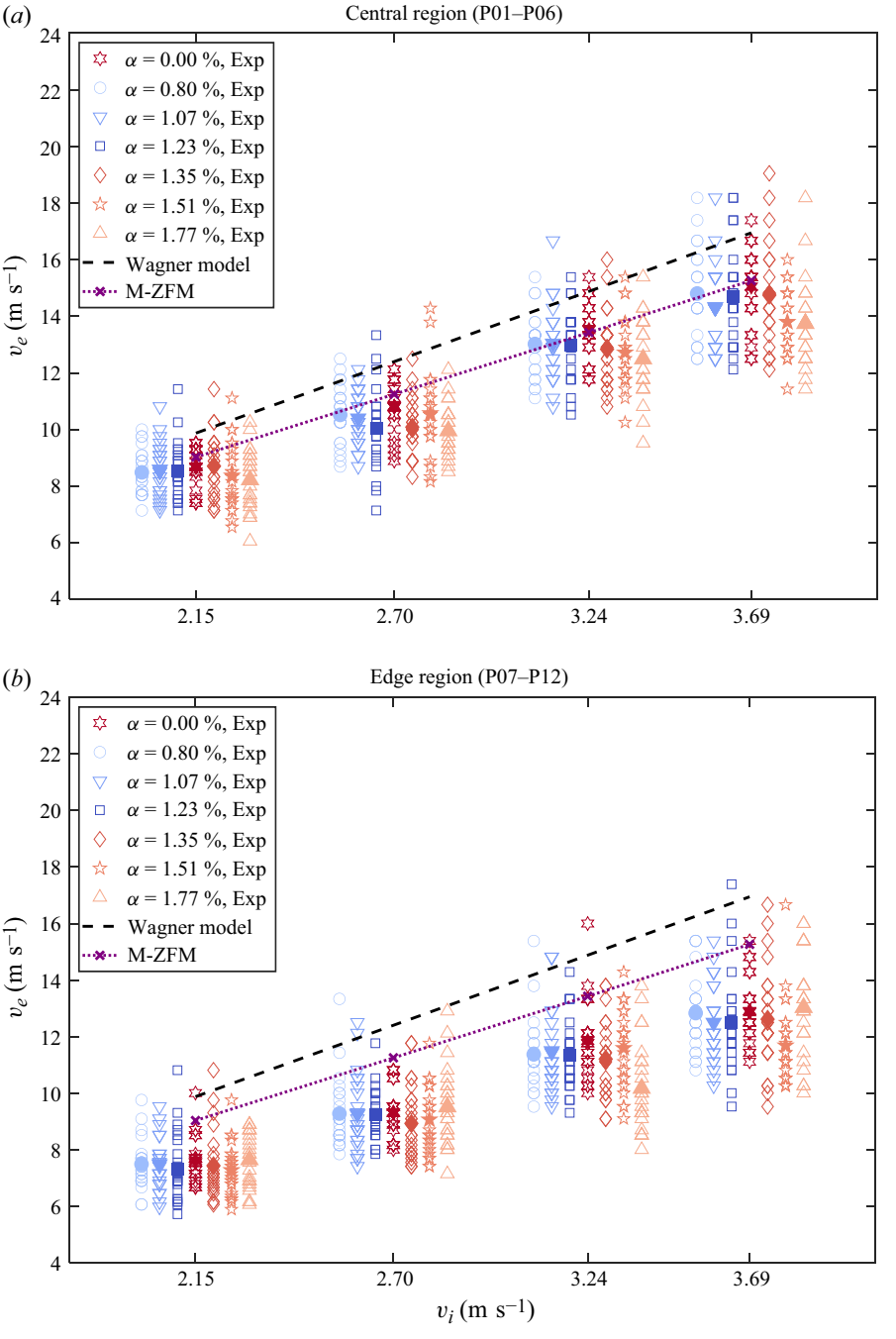


Figure 12. Relationship between the wet surface expansion velocity v_e and water-entry velocity v_i at varied void fractions. Panel (*a*) shows the data for sensors P01–P06 (central region), while panel (*b*) shows the data for sensors P07–P12 (edge region). Experimental results are represented by hollow markers (five repeated tests for each condition) and solid markers (mean values). The dashed black line represents theoretical predictions from Wagner model, and the dotted purple line corresponds to the results from the M-ZFM. The expansion velocity predicted by M-ZFM in the central region keeps constant across all void fractions. Notably, for each experiment at a specific void fraction and entry velocity, five expansion velocities (v_e^{12}, v_e^{23}, v_e^{34}, v_e^{45}, v_e^{56}) in the central region are grouped under a single marker type, with same grouping also applied to edge region sensors aligned parallel to the centreline.

https://doi.org/10.1017/jfm.2025.10983 Published online by Cambridge University Press

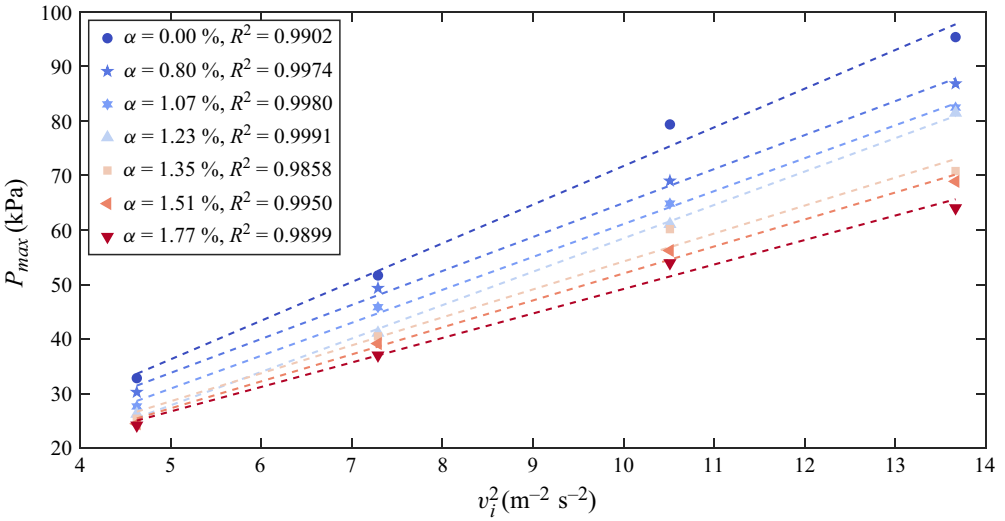


Figure 13. Variation of peak impact pressure P_{max} recorded by sensor P01 relative to the square of the entry velocity v_i^2 at varied void fractions. For each test condition, the P_{max} was calculated by averaging the records at all the tests carried out. The linear relationship between P_{max} and v_i^2 remains evident at all tested void fractions, while the slope of this linear correlation decreases with increasing void fraction. The dashed lines represent the linear fit of the scatter data for each corresponding void fraction, with the fitting coefficient R^2 provided in the legend.

mixture, thereby reducing the peak pressures. This further validates the rationality and necessity of integrating aeration effects into the theoretical model proposed in § 3. Further analysis was conducted to quantify the influence of aeration on peak impact pressures. As demonstrated in figure 13, P_{max} exhibits a marked reduction with increasing void fraction, with the reduction becoming more pronounced at higher aeration level. For instance, at $v_i = 3.69\ \mathrm{m\ s^{-1}}$, the P_{max} decreases from 95.35 kPa in pure water to 64.04 kPa at $\alpha = 1.77\ \%$, corresponding to a 32.8 % decrease.

This reduction can be attributed to the presence of entrained air, which provides an effective air cushioning effect. Upon impact, the entrained gas compresses and absorbs a portion of the impact energy, thereby acting as a compliant cushion between the wedge and the liquid. This mechanism reduces the instantaneous force on the wedge, resulting in a lower peak pressure. Meanwhile, in a water-entry event, the dominant mechanism of force generation is the fluid's inertia (added mass) resisting the body's motion. With a lower density fluid due to air voids, the effective added mass is reduced, meaning the fluid offers less resistance to the wedge's penetration. This fundamentally leads to smaller impact pressures. Both effects contribute to a reduced peak impact pressure in aerated water.

In addition, the sound speed c_m drops sharply as the void fraction increases in an aerated mixture. Upon impact of the wedge, the initial pressure disturbance propagates into the fluid at speed c_m. Over a short time interval Δt immediately after impact, the disturbance travels a distance $c_m \Delta t$ and accelerates the fluid in that region of mass $M_f = \rho c_m A \Delta t$ beneath the patch of area A. Equating the momentum gained by this fluid ($M_f v_i$) with the impulse delivered by the pressure ($P_a A \Delta t$, where P_a is the average pressure), the average pressure can be obtained as

$$P_a = \rho c_m v_i, \tag{4.4}$$

https://doi.org/10.1017/jfm.2025.10983 Published online by Cambridge University Press

which is often referred to as the acoustic pressure for the impact. This analysis illustrates that a reduction in c_m directly lowers the impedance $Z_m = \rho c_m$ and hence yields a lower attainable peak pressure P_a for a given impact velocity v_i. Although the acoustic pressure P_a is rarely observed in experiments due to the more complex real-world conditions, it links the sound speed to impact pressure and provides a mechanistic rationale for why entrained air leads to a reduction of the peak impact pressure P_{max} in aerated water.

In the experimental set-up employed in this study, the evolution of impact pressures was observed to follow the inertial scaling even under aerated conditions, which formed the basis for comparing experimental results with theoretical predictions. Figure 14 displays the non-dimensionalised peak pressure measured at sensors P01–P06 for three representative cases: pure water ($\alpha = 0.00\,\%$), low void fraction ($\alpha = 0.80\,\%$) and high void fraction ($\alpha = 1.77\,\%$), alongside standard deviations from repeated trials. Theoretical predictions from the O-ZFM (pure water only), M-ZFM, M-OLM, M-MLM and M-GWM are also presented. For pure water, the O-ZFM not only overestimated the impact loads at sensors P01 and P02 (as also shown in figure 9) but also overpredicted the load at P03 while underpredicting P06. This misalignment would be more pronounced under aerated conditions, where traditional models neglecting the aeration effect significantly overestimated impact pressures.

A clear pattern emerged from the data of all six sensors, indicating that peak pressures initially increased with the vertical position of the sensor, reached a maximum at sensor P02 and subsequently decreased toward higher positions (P06). All modified models successfully captured this characteristic pressure distribution. One can observe that, in pure water, experimental peak pressures exhibited low variability and high repeatability. In contrast, greater variance in the peak pressure was introduced by aeration because the bubble field generated by the bubble generator cannot be perfectly consistent in each repeated test. However, despite this variability, the aerated impact pressure was generally lower than pure water, a trend reproduced by the proposed aeration-inclusive models. The modified models proposed in this study, which account for the aeration effect, performed well in predicting the peak impact pressures at P01–P06 in aerated conditions, thereby validating the effectiveness of the model. Among the analytical models, the M-MLM appeared to provide the most accurate results. This improved prediction of hydrodynamic pressure was achieved by considering the nonlinear effects associated with the quadratic term of the Bernoulli equation and the realistic geometry of the wetted surface.

4.4. *Impact pressure impulse and duration*

The impact pressure measured directly on the wedge is the most basic indicator to describe the impact event. However, in many cases, impact pressure can exhibit great randomness between tests conducted at the same conditions. As previously mentioned, this variability can stem from the limited temporal resolution of the pressure sensors or from the aeration effect. It has been suggested that the time-integrated pressure impulse is more critical for quantifying local damage, owing to its improved repeatability and predictability (Wu *et al.* 2024). Additionally, Manjula & Sannasiraj (2019) found from wave impacts on a slender cylindrical member that waves producing high pressures over short durations were less significant for structural damage than those producing lower pressures over longer durations. Therefore, the safety of structure is not only determined by the peak impact pressure but also by the impact duration. Since the pressure impulse is closely related to the impact duration, the characteristics of impact pressure duration are investigated first in this section, followed by an analysis of the pressure impulse.

https://doi.org/10.1017/jfm.2025.10983 Published online by Cambridge University Press

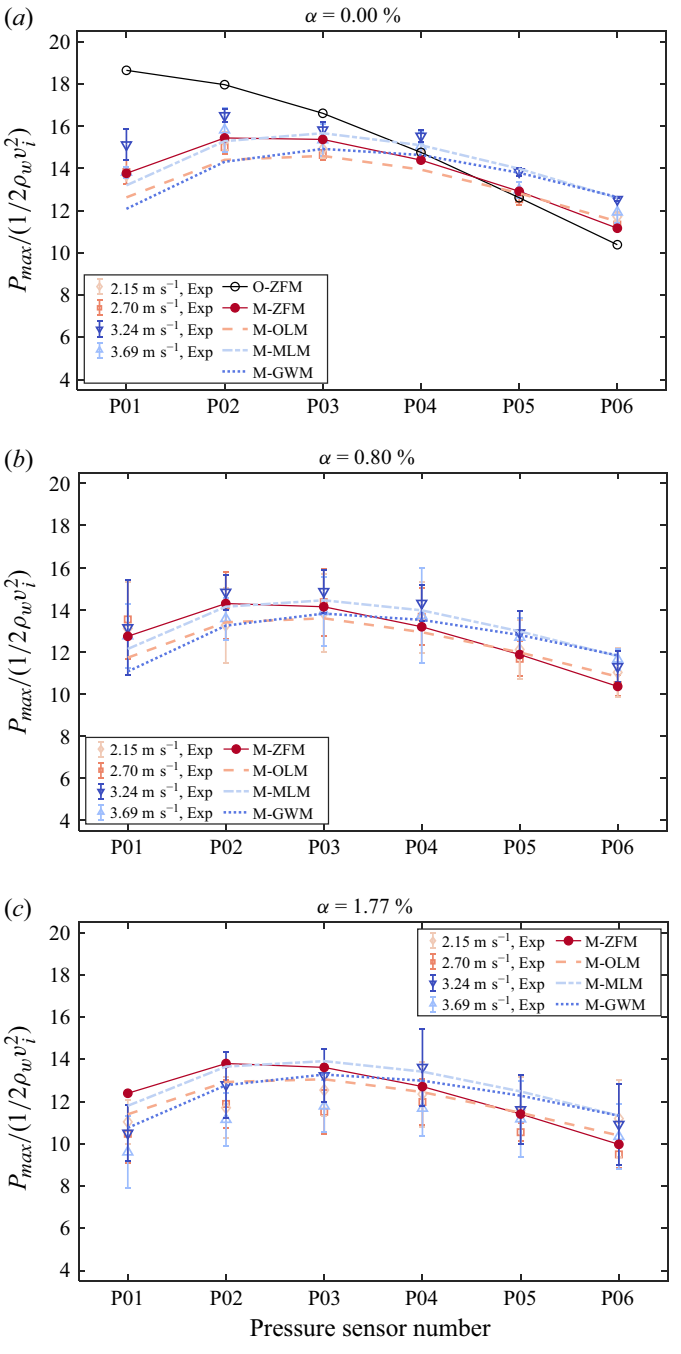


Figure 14. Variation of the dimensionless maximum pressure measured by sensors P01–P06 in different void fractions and entry velocities, with error bars representing the standard deviations of the repeated tests. Sensors P01–P06 were evenly distributed along the centreline of the wedge, maintaining a 20 mm spacing between adjacent sensors. The theoretical predictions from the O-ZFM model (represented by solid black lines for pure water) and the modified models (M-ZFM, M-OLM, M-MLM and M-GWM) are shown with different coloured lines: red solid line for M-ZFM, orange dashed line for M-OLM, light blue dash-dotted line for M-MLM and blue dotted line for M-GWM.

https://doi.org/10.1017/jfm.2025.10983 Published online by Cambridge University Press

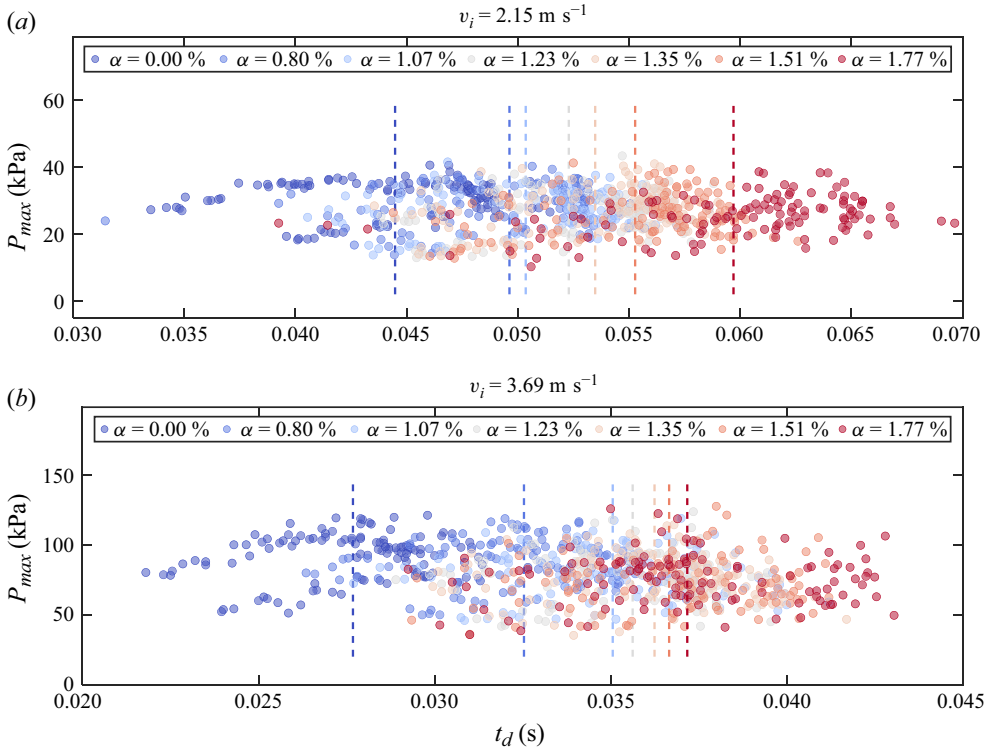


Figure 15. Distributions of impact pressure duration under different void fractions. The vertical dashed lines in each panel correspond to the mean impact duration for each void fraction.

The distribution of the impact pressure duration at a range of void fractions is presented in figure 15, denoted by circular markers in different colours. The vertical dashed lines in corresponding colours indicate the mean duration for each α, providing a clear reference for comparing the durations at varying aeration levels. A clear trend is observed that the mean duration gradually increased with higher void fraction. As shown in figure 15(*a*), the durations rose from 0.04 to 0.05 s in pure water to predominantly exceed 0.05 s at $\alpha = 1.77$ %. This increase in duration can be explained by the reduced inertial resistance of the aerated water. With entrained air lowering the fluid's effective density, the added mass is reduced, and the fluid provides less resistance to the wedge's penetration. The wedge penetrates slightly further into the fluid before decelerating, thereby extending the duration of the impact event. In essence, aeration leads to a lower instantaneous impact force but allows the impact to last longer, distributing the energy over a longer time.

Additionally, the reduction in c_m also slows the establishment of the pressure field. The characteristic time for pressure wave to communicate across a length L is the acoustic time scale

$$\tau_a = \frac{L}{c_m}, \tag{4.5}$$

where L is a characteristic length (e.g. the equivalent depth of the added-mass region). Thus, a smaller c_m in more aerated water yields a larger τ_a, producing a more gradual rise and a broader pulse. This also explains why the aerated cases exhibit longer-lasting pressure pulses compared with the pure water cases. Furthermore, a comparison between

https://doi.org/10.1017/jfm.2025.10983 Published online by Cambridge University Press

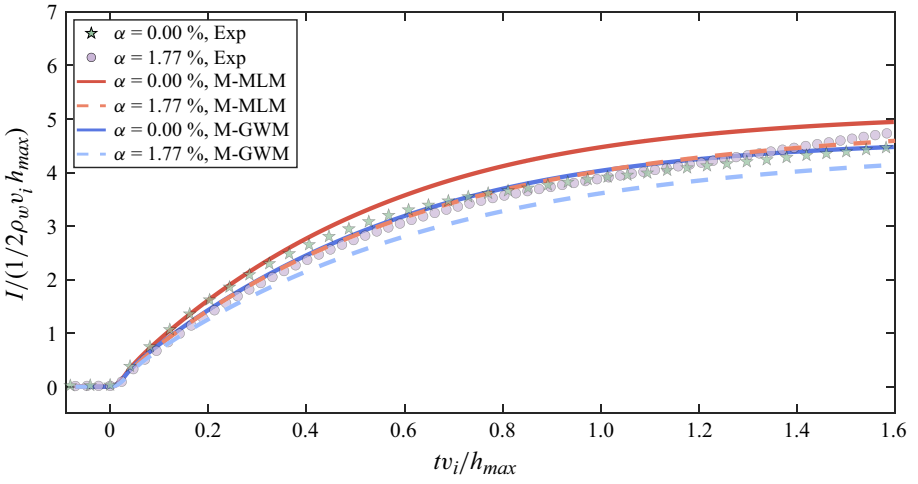


Figure 16. Temporal evolution of normalised impact impulse ($I/(1/2)\rho_w v_i h_{max}$) at sensor P01 comparing experimental measurements (Exp) with predictions from the M-MLM and M-GWM models under two aeration conditions: pure water ($\alpha = 0.00\,\%$) and aerated water ($\alpha = 1.77\,\%$). For clarity, symbols are shown every 10 samples.

figure 15(*a*) and 15(*b*) reveals that, as expected, impact durations decreased with increasing water-entry velocity.

The impact pressure impulse, as a parameter combining both impact pressure and duration, serves as a direct indicator of the energy exerted on the wedge during the water-entry process. Figure 16 illustrates the evolution of the dimensionless impulse as a function of dimensionless time for pure water and high-aeration water ($\alpha = 1.77\,\%$). Predictions from the M-MLM and M-GWM are also presented, as these models demonstrate better accuracy in predicting peak values and account for the realistic wedge geometry.

For the experimental results, the impulse in aerated water remained lower than that in pure water in the pre-peak phase. After a certain point following the peak (approximately at $tv_i/h_{max} = 1$), the pressure impulse under aerated conditions surpassed that of pure water. This may arise from the prolonged impact duration caused by the presence of gas. In contrast, it is observed that the predicted impulse in aerated water was consistently lower than that in pure water for both the M-MLM and M-GWM. This discrepancy could be explained by the assumption in the models that the gas bubbles are uniformly distributed and rise at the same velocity, which is determined based on the experimentally measured average rise velocity of the bubbles near the surface. However, experimentally observed bubble volumetric expansion and inter-bubble collision processes may induce variations in terminal rise velocities. According to the momentum theorem, the individual momentum of the bubbles also affects the total impulse applied to the wedge, potentially leading to an underestimation of the impulse prediction for aerated water. Generally, in pure water, both M-MLM and M-GWM provided good agreement with the experimental evolution of the impact impulse. Comparative analysis revealed that under aerated conditions, the M-MLM model outperformed the M-GWM in predicting the impact impulse evolution.

Figure 17 depicts the dimensionless impact pressure impulse measured by sensors P01–P06 against the void fractions. Error bars representing the standard deviation for five repeated tests are provided at the top of the histogram columns. Spatially, the magnitude of the impulse declined with the location being away from the wedge's keel, due to the progressive velocity reduction of the wedge during water entry. Comparing figures 14

https://doi.org/10.1017/jfm.2025.10983 Published online by Cambridge University Press

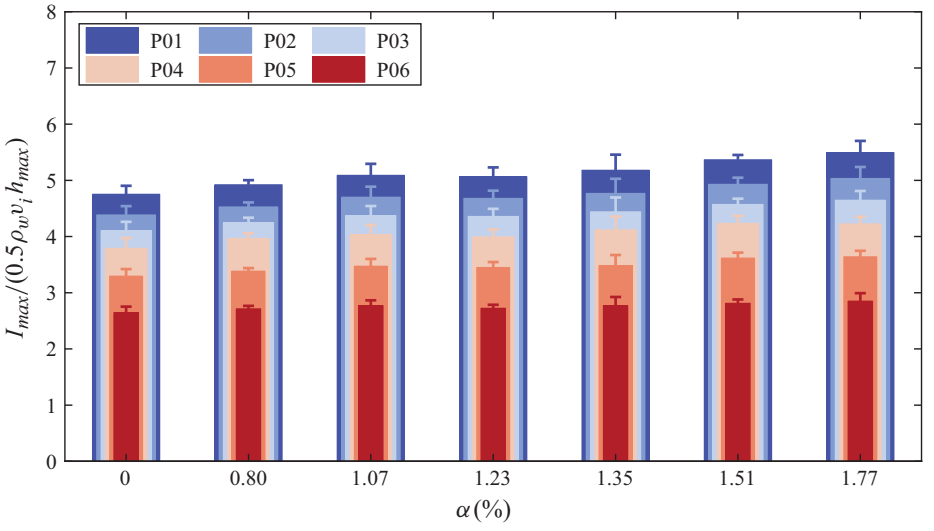


Figure 17. Variation of the dimensionless maximum impact impulse at different void fractions for sensors P01 to P06, with error bars at the top of the columns indicating the standard deviation from repeated measurements.

and 17, it is evident that the variation of impact impulse from repeated experiments was much less than that of peak pressure, for both pure and aerated water entry. Furthermore, there is no reduction of the impact pressure impulses from pure water to aerated water entry. Indeed, a slight increase was even observed at certain sensor locations, such as P01. Introducing gas into pure water reduces the wedge's peak impact pressure and prolongs the impact load duration. But, by integrating the pressure over time, these two opposing effects partially compensated for each other, resulting in an almost stable impulse. At higher aeration levels, the effect of extended duration became more pronounced, leading to an increased total load applied to the wedge, which may pose a greater risk to the structure. This finding aligns with the conclusions of Cuomo, Shimosako & Takahashi (2009) that less intense but longer-lasting wave loads may be more critical for the deck than more intense but shorter-lasting impacts, based on the research involving wave-induced impact loads on bridges.

5. Conclusions

The present study combines carefully controlled experiments and improved theoretical models to investigate the influence of void fraction and impact velocity on water-entry impact loads. A wedge impactor featuring a deadrise angle of 20° was dropped into pure and aerated water, considering seven different void fractions and four distinct impact velocities. To account for the aeration effect, classical pure water-entry models (ZFM, OLM, MLM and GWM) are extended as four modified models (M-ZFM, M-OLM, M-MLM and M-GWM). This is the first study that systematically modifies and compares multiple classical water-entry impact models in pure and aerated conditions. This theoretical development is both novel and useful, as it provides engineers and researchers a set of ready-to-use models for predicting aerated impact loads. The aerated water is treated as a homogeneous mixture of compressible gas and weakly compressible liquid. The time-dependent void fraction expression is developed based on the added-mass concept. The three-dimensional flow effects and area-averaged pressure are also considered to

https://doi.org/10.1017/jfm.2025.10983 Published online by Cambridge University Press

improve prediction accuracy. A detailed investigation of the aeration effect on impact pressure characteristics, including pressure time series, peak pressure, impact duration and pressure impulse, was carried out. Additionally, the expansion velocity of the wetted surface was inferred from the pressure data and compared with the theoretical predictions. The predictive accuracy of the proposed modified models was validated against the experimental results.

For the time evolution and spatial distribution of the impact pressure, significant three-dimensional effects were identified, particularly near the wedge edges where peak pressures were lower and delayed relative to the centreline. This highlights the importance of including three-dimensional corrections in theoretical models for finite-width wedges. The modified models exhibited excellent agreement with the experimental temporal evolution of impact pressure. Among them, M-MLM provided accurate peak pressure predictions in pure and aerated water, while M-GWM exhibited the best overall performance in capturing the post-peak behaviours. The wetted surface expansion velocities derived from the pressure data revealed clear spatial variations, with consistently lower values near the wedge edges due to lateral dispersion of the jet momentum. Moreover, it remained nearly constant at different aeration levels, and the M-ZFM predictions agreed well with the experimental data, indicating that aeration-induced surface disturbances were within an acceptable range.

Peak impact pressures were observed to scale with the square of the entry velocity in both pure and aerated conditions, indicating the inertia-dominated processes. Increasing the void fraction resulted in a notable reduction in peak pressures, primarily attributed to the lowered effective fluid density and the cushioning effect introduced by the gas–liquid mixture. Furthermore, the time-integrated pressure impulses showed significantly lower variability across repeated tests, remaining stable or even exhibiting a slight increase in highly aerated water. This phenomenon can be explained by the compensating effects of reduced peak pressure and prolonged impact duration associated with aeration. This finding draws attention to the risk that prolonged lower-magnitude impacts may pose an equivalent or even greater threat to structural integrity than short-duration high-magnitude impacts.

The combined experimental and theoretical advancements in this work offer new fundamental insights and practical implications in aerated water entry. However, a limitation lies in the simplified treatment of bubble dynamics within the theoretical models, which assumes a uniform spatial distribution of gas bubbles, a constant bubble rise velocity and neglects the detailed behaviour of individual bubbles. Future research incorporating more realistic descriptions of bubble dynamics would further enhance the accuracy and predictive capability of impact load models in mixed air–water environments. Additionally, expanding the velocity range in future experimental investigations will further substantiate the general applicability and robustness of the proposed models.

Acknowledgements. The authors acknowledge Y. Chen for assisting with the experiment. They also wish to express their gratitude to Professor J. Xiong and Professor X. Tian for the invaluable support.

Funding. This study is supported by the National Natural Science Foundation of China (Grant No. 52031006).

Declaration of interests. The authors report no conflict of interest.

References

Abrate, S. 2011 Hull slamming. *Appl. Mech. Rev.* **64** (6), 060803.

Aghaei, A., Schimmels, S., Schlurmann, T. & Hildebrandt, A. 2020 Numerical investigation of the effect of aeration and hydroelasticity on impact loading and structural response for elastic plates during water entry. *Ocean Engng* **201**, 107098.

https://doi.org/10.1017/jfm.2025.10983 Published online by Cambridge University Press

BAARHOLM, R. 2009 Experimental and theoretical study of three-dimensional effects on vertical wave-in-deck forces. *Intl Conf. Offshore Mech. Arctic Engng* **43468**, 451–459.
BARJASTEH, M., ZERAATGAR, H. & JAVAHERIAN, M.J. 2016 An experimental study on water entry of asymmetric wedges. *Appl. Ocean Res.* **58**, 292–304.
BELDEN, J., SPEIRS, N.B., HELLUM, A.M., JONES, M., PAOLERO, A.J. & TRUSCOTT, T.T. 2023 Water entry of cups and disks. *J. Fluid Mech.* **963**, A14.
BELDEN, J., SPEIRS, N., HELLUM, A., LOUBIMOV, G. & TRUSCOTT, T.T. 2024 Water impact: when a sphere becomes flat. *Phys. Rev. Lett.* **133** (3), 034002.
BREDMOSE, H., PEREGRINE, D.H. & BULLOCK, G.N. 2009 Violent breaking wave impacts. Part 2: modelling the effect of air. *J. Fluid Mech.* **641**, 389–430.
BULLOCK, G.N., OBHRAI, C., PEREGRINE, D.H. & BREDMOSE, H. 2007 Violent breaking wave impacts. Part 1: results from large-scale regular wave tests on vertical and sloping walls. *Coast. Engng* **54** (8), 602–617.
CHUANG, S.L. 1966 Slamming of rigid wedge-shaped bodies with various deadrise angles. *Tech. Rep.* No. 2268.
CHUANG, W.L. 2022 Experimental investigation on fluid kinematics and impact pressure of flat plate impacts on pure and aerated water. *Ocean Engng* **266**, 112837.
CUOMO, G., SHIMOSAKO, K. & TAKAHASHI, S. 2009 Wave-in-deck loads on coastal bridges and the role of air. *Coast. Engng* **56** (8), 793–809.
DEANE, G.B. & STOKES, M.D. 2002 Scale dependence of bubble creation mechanisms in breaking waves. *Nature* **418** (6900), 839–844.
DIAS, F., DUTYKH, D. & GHIDAGLIA, J.M. 2010 A two-fluid model for violent aerated flows. *Comput. Fluids* **39** (2), 283–293.
DOBROVOL'SKAYA, Z.N. 1969 On some problems of similarity flow of fluid with a free surface. *J. Fluid Mech.* **36** (4), 805–829.
ELHIMER, M., EL MALKI ALAOUI, A., GABILLET, C. & JACQUES, N. 2022 Measurements of pressure during the forced water entry of a cone into pure and aerated water. *J. Fluid. Struct.* **113**, 103605.
ELHIMER, M., JACQUES, N., EL MALKI ALAOUI, A. & GABILLET, C. 2017 The influence of aeration and compressibility on slamming loads during cone water entry. *J. Fluid. Struct.* **70**, 24–46.
ERMANYUK, E.V. & OHKUSU, M. 2005 Impact of a disk on shallow water. *J. Fluid. Struct.* **20** (3), 345–357.
FAN, Y., JAIN, U. & VAN DER MEER, D. 2024 Air-cushioning below an impacting wave-structured disk: free-surface deformation and slamming load. *Phys. Rev. Fluids* **9** (1), 010501.
GUO, Y., XIAO, L., TENG, X., KOU, Y. & LIU, J. 2020 Processing method and governing parameters for horizontal wave impact loads on a semi-submersible. *Mar. Struct.* **69**, 102673.
HAN, B., LI, H., ZHANG, B., ZOU, J. & ZHAO, W. 2024 Experimental investigation of slamming characteristics of stiffened elastic wedges with different deadrise angles: Part I–Slamming pressure. *Ocean Engng* **303**, 117728.
HONG, Y., WANG, B. & LIU, H. 2021 Experimental and numerical study on hydrodynamic impact of a disk in pure and aerated water. *Proc. Inst. Mech. Engng M* **235** (1), 152–164.
IAFRATI, A. 2016 Experimental investigation of the water entry of a rectangular plate at high horizontal velocity. *J. Fluid Mech.* **799**, 637–672.
JAIN, U., GAUTHIER, A.F., LOHSE, D. & VAN DER MEER, D. 2021 Air-cushioning effect and Kelvin–Helmholtz instability before the slamming of a disk on water. *Phys. Rev. Fluids* **6** (4), L042001.
JAIN, U., NOVAKOVIĆ, V., BOGAERT, H. & VAN DER MEER, D. 2022 On wedge-slamming pressures. *J. Fluid Mech.* **934**, A27.
VON KARMAN, T. 1929 The impact on sea plane floats during landing. *Tech. Rep.* No. NACA-TN-321. Aerodynamical Institute 776 of the Technical High School, Aachen, 1929.
KHABAKHPASHEVA, T.I., KOROBKIN, A.A. & MALENICA, S. 2013 Fluid impact onto a corrugated panel with trapped gas cavity. *Appl. Ocean Res.* **39**, 97–112.
KOROBKIN, A. 2004 Analytical models of water impact. *Eur. J. Appl. Math.* **15** (6), 821–838.
KOROBKIN, A.A. 2006 Two-dimensional problem of the impact of a vertical wall on a layer of a partially aerated liquid. *J. Appl. Mech. Tech. Phys.* **47**, 643–653.
LIN, M.C. & SHIEH, L.D. 1997 Simultaneous measurements of water impact on a two-dimensional body. *Fluid Dyn. Res.* **19** (3), 125.
LOGVINOVICH, G.V. 1972 *Hydrodynamics of Free-Boundary Flows [M]*. Israel Program for Scientific Translations.
LU, W., WU, X. & ZHA, R. 2024 Numerical study on the motion characteristics of free fall lifeboats entering calm water and rough sea. *Phys. Fluids* **36** (9), 097102.

https://doi.org/10.1017/jfm.2025.10983 Published online by Cambridge University Press

MA, Z.H., CAUSON, D.M., QIAN, L., MINGHAM, C.G., MAI, T., GREAVES, D. & RABY, A. 2016 Pure and aerated water entry of a flat plate. *Phys. Fluids* **28** (1), 016104.

MAI, T., MAI, C., RABY, A. & GREAVES, D.M. 2019 Aeration effects on water-structure impacts: Part 1. Drop plate impacts. *Ocean Engng* **193**, 106600.

MANJULA, R. & SANNASIRAJ, S.A. 2019 Response of a slender cylindrical member under breaking wave impact. *J. Hydrodyn.* **31**, 345–357.

MELVILLE, W.K. 1996 The role of surface-wave breaking in air-sea interaction. *Annu. Rev. Fluid Mech.* **28**, 279–321.

MILLER, S.T., JASAK, H., BOGER, D.A., PATERSON, E.G. & NEDUNGADI, A. 2013 A pressure-based, compressible, two-phase flow finite volume method for underwater explosions. *Comput. Fluids* **87**, 132–143.

PEREGRINE, D.H. & THAIS, L. 1996 The effect of entrained air in violent water wave impacts. *J. Fluid Mech.* **325**, 377–397.

PETERS, I.R., VAN DER MEER, D. & GORDILLO, J.M. 2013 Splash wave and crown breakup after disc impact on a liquid surface. *J. Fluid Mech.* **724**, 553–580.

PLUMERAULT, L.-R., ASTRUC, D., VILLEDIEU, P. & MARON, P. 2012 A numerical model for aerated-water wave breaking. *Intl J. Numer. Meth. Fluids* **69** (12), 1851–1871.

PUMPHREY, H.C. & ELMORE, P.A. 1990 The entrainment of bubbles by drop impacts. *J. Fluid Mech.* **220**, 539–567.

SAUREL, R. & ABGRALL, R. 1999 A simple method for compressible multifluid flows. *SIAM J. Sci. Comput.* **21** (3), 1115–1145.

SEMENOV, Y.A. & IAFRATI, A. 2006 On the nonlinear water entry problem of asymmetric wedges. *J. Fluid Mech.* **547**, 231–256.

SHAN, M., XIAO, L., KOU, Y., WU, W. & LI, K. 2025 Wave run-up and secondary load cycle on a rounded square column in focused waves. *Phys. Fluids* **37** (2), 023369.

SILBERMAN, E. 1957 Sound velocity and attenuation in bubbly mixtures measured in standing wave tubes. *J. Acoust. Soc. Am.* **29** (8), 925–933.

TASSIN, A., JACQUES, N., EL MALKI ALAOUI, A., NÊME, A. & LEBLÉ, B. 2010 Assessment and comparison of several analytical models of water impact. *Intl J. Multiphys.* **4** (2), 125–140.

VERHAGEN, J.H.G. 1967 The impact of a flat plate on a water surface. *J. Ship Res.* **11** (04), 211–223.

WAGNER, H. 1932 Über stoß-und gleitvorgänge an der oberfläche von flüssigkeiten. *ZAMM* **12** (4), 193–215.

WANG, J. & FALTINSEN, O. 2017 Improved numerical solution of Dobrovol'skaya's boundary integral equations on similarity flow for uniform symmetrical entry of wedges. *Appl. Ocean Res.* **66**, 23–31.

WEN, X., QU, Q., LIU, P. & HU, T. 2024 A general solution for the water entry of an arbitrary curved wedge. *Ships Offshore Struc.* 1–17. https://www.tandfonline.com/doi/full/10.1080/17445302.2024.2403182

WU, J. 2000 Bubbles produced by breaking waves in fresh and salt waters. *J. Phys. Oceanogr.* **30** (7), 1809–1813.

WU, W., LIU, M., XIAO, L., SHAN, M., KOU, Y., LI, K. & GUO, J. 2024 Experimental study of wave impact pressure impulse and characteristic pressure on the fixed four-rounded-square-column array in focused waves. *Ocean Engng* **311**, 118829.

WU, W., XIAO, L., KOU, Y. & LIU, M. 2025 Research on impact pressures in aerated water entry of a symmetrical wedge. *J. Fluid Mech.* **1010**, A4.

YAMAMOTO, Y., OHTSUBO, H. & KOHNO, Y. 1984 Water impact of wedge model. *J. Soc. Naval Arch. Japan* **1984** (155), 236–245.

YETTOU, E.M., DESROCHERS, A. & CHAMPOUX, Y. 2006 Experimental study on the water impact of a symmetrical wedge. *Fluid Dyn. Res.* **38** (1), 47.

YETTOU, E.M., DESROCHERS, A. & CHAMPOUX, Y. 2007 A new analytical model for pressure estimation of symmetrical water impact of a rigid wedge at variable velocities. *J. Fluid. Struct.* **23** (3), 501–522.

ZHANG, N., XIAO, L., CHENG, Z., WEI, H. & CHEN, G. 2024 Classification of breaking wave impact loads on a fixed surface-piercing square column with an overhanging deck. *Coast. Engng* **193**, 104570.

ZHAO, R. & FALTINSEN, O. 1993 Water entry of two-dimensional bodies. *J. Fluid Mech.* **246**, 593–612.

https://doi.org/10.1017/jfm.2025.10983 Published online by Cambridge University Press